

DESIGN AND DEVELOPMENT OF SELF-POWERED
PRESSURE SENSORS BASED ON TRIBOELECTRIC
PRINCIPLE

GOH QI LUN

MASTER OF ENGINEERING SCIENCE

LEE KONG CHIAN FACULTY OF ENGINEERING
AND SCIENCE
UNIVERSITI TUNKU ABDUL RAHMAN
APRIL 2022

**DESIGN AND DEVELOPMENT OF SELF-POWERED PRESSURE
SENSORS BASED ON TRIBOELECTRIC PRINCIPLE**

By

GOH QI LUN

A dissertation submitted to the Department of Electrical and Electronic
Engineering,
Lee Kong Chian Faculty of Engineering and Science,
Universiti Tunku Abdul Rahman,
in partial fulfillment of the requirements for the degree of
Master of Engineering Science
April 2022

ABSTRACT

Design and Development of Self-powered Pressure Sensors Based on Triboelectric Principle

GOH QI LUN

Triboelectric nanogenerator (TENG) is a promising approach in achieving a self-powered pressure sensing application. However, most reported TENG is usually developed using solid and rigid materials which do not comply with soft and irregular surfaces such as human skin and soft robotic, obstructing it from performing conformal sensing for a wearable device and soft robotic application. One of the methods to resolve the problems mentioned above is to develop the TENG with stretchable materials. To explore triboelectric based pressure sensing on soft and irregular surfaces, this dissertation reported self-powered pressure sensors fabricated from soft and stretchable materials and evaluated their performance for both human pressure sensing and soft robotic application for pick-and-place operation.

Polydimethylsiloxane (PDMS) elastomer and deionised water are proposed as triboelectric materials to develop our first soft and wearable self-powered pressure sensor. The sensor achieved a sensitivity of 0.20 mV/kPa for fingertip pressure sensing and was successfully used for human-machine interface (HMI) application as a proof of principle in demonstrating the sensor's sensitivity. It is also highly compressible and flexible, preventing cracking compared to the traditional solid-state triboelectric sensors.

However, we found that the output voltage highly relies on compression stroke at the water chamber in our first sensor design, limiting the sensor from detecting larger pressure input such as hand tapping motion. Therefore, in our second approach, we introduced a sponge-like structure in the elastomer to increase the contacted surface area of the triboelectric materials. With this modification, the sensing performance of the pressure sensor has been improved by an increased factor of 40 times when harvesting energy from the human hand tapping motion. This improvement allows the TENG sensor to generate a momentary power density of $99.47 \mu\text{W}/\text{cm}^2$ and light up several LEDs. Furthermore, eutectic gallium-indium (EGAI_n) was mixed in the elastomer to make it a conductive medium. Thus, the necessity for solid electrodes can be eliminated.

Upon exploring the capability of the eutectic gallium-indium (EGAI_n) made sponge-like pressure sensor in human pressure sensing, we further leveraged it to a pneumatic actuated soft robotic gripper to perform object recognition in pick and place operation. The pressure sensor is characterised with a sensitivity of 43 mV/kPa. To detect the bending angle of the fingers in the soft gripper, we develop bending sensors using the same material and principle as the pressure sensor. The collected signals were then used to recognize objects through the support vector machine (SVM) learning approach. The accuracy of the soft gripper can be achieved up to 91.6%. The developed self-powered and soft sensor has successfully proven its ability to detect pressure with different magnitudes and operating frequencies for soft robotic applications.

ACKNOWLEDGEMENTS

I would like to thank everyone who had contributed to the successful completion of this project. I would like to express my gratitude to my research supervisors, Dr. Chee Pei Song and Prof. Lim Eng Hock for their invaluable advice, guidance, and their enormous patience throughout the development of the research.

In addition, I would also like to express my gratitude to my loving parents and friends who had helped and given me encouragement to complete my dissertation when I was facing many obstacles. Additionally, I would like to specially thank Ir. Danny Ng Wee Kiat and Dr. King Yeong Jin, for guiding me in the experiments, which helped in this project.

APPROVAL SHEET

This dissertation entitled “**DESIGN AND DEVELOPMENT OF SELF-POWERED PRESSURE SENSORS BASED ON TRIBOELECTRIC PRINCIPLE**” was prepared by GOH QI LUN and submitted as partial fulfilment of the requirements for the degree of Master of Engineering Science at Universiti Tunku Abdul Rahman.

Approved by:



(Dr. CHEE PEI SONG)

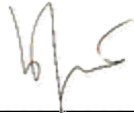
Date: 24/4/2022

Associate Professor/Supervisor

Department of Mechatronics & Biomedical Engineering

Lee Kong Chian Faculty of Engineering & Science

Universiti Tunku Abdul Rahman



(Prof. Dr. LIM ENG HOCK)

Date: 24/4/2022

Professor/Co-supervisor

Department of Electrical & Electronic Engineering

Lee Kong Chian Faculty of Engineering & Science

Universiti Tunku Abdul Rahman

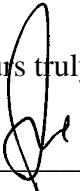
**LEE KONG CHIAN FACULTY OF ENGINEERING AND SCIENCE
UNIVERSITI TUNKU ABDUL RAHMAN**

Date: 24 April 2022

SUBMISSION OF DISSERTATION

It is hereby certified that **GOH QILUN** (ID No: **20UEM00165**) has completed this dissertation entitled “**DESIGN AND DEVELOPMENT OF SELF-POWERED PRESSURE SENSORS BASED ON TRIBOELECTRIC PRINCIPLE**” under the supervision of Dr. Chee Pei Song (Supervisor) from the Department of Mechatronics & Biomedical Engineering, Lee Kong Chian Faculty of Engineering and Science (FES), and Prof. Dr. Lim Eng Hock (Co-Supervisor) from the Department of Electrical and Electronic Engineering, Lee Kong Chian Faculty of Engineering and Science (FES).

I understand that University will upload softcopy of my dissertation in pdf format into UTAR Institutional Repository, which may be made accessible to UTAR community and public.

Yours truly,


(GOH QILUN)

DECLARATION

I hereby declare that the dissertation is based on my original work except for quotations and citations which have been duly acknowledged. I also declare that it has not been previously or concurrently submitted for any other degree at UTAR or other institutions.

Name GOH QILUN

Date 24 APRIL 2022

TABLE OF CONTENTS

	Page
ABSTRACT	ii
ACKNOWLEDGEMENTS	iv
APPROVAL SHEET	v
DECLARATION	vii
TABLE OF CONTENTS	viii
LIST OF TABLES	xii
LIST OF FIGURES	xiii
LIST OF ABBREVIATIONS	xvii
CHAPTER	
1 INTRODUCTION	1
1.1 Background	1
1.2 Problem Statements	3
1.3 Research Questions	4
1.4 Aim and Objectives	5
1.5 Dissertation Outline	5
2 LITERATURE REVIEW	8
2.1 Self-Powered Technology	8
2.1.1 Piezoelectric Generators (PGs) Vs. Triboelectric Nanogenerators (TENGs)	9
2.2 Introduction of Triboelectric Nanogenerators (TENGs)	10
2.2.1 Triboelectric Effect	10
2.2.2 Triboelectric Series	12
2.2.3 Fundamental Operation Modes of TENG	13
2.3 Modification to improve TENG's performance	21
2.3.1 Physical Modification of TENG Layers	22
2.3.2 Material Selection for TENG Layers	26

2.3.3	Operating Parameters: Frequency, Movement Amplitude, and Input Pressure	26
2.3.4	Environment Parameters	28
2.4	Stretchable Materials in TENG Sensor	29
2.4.1	Polydimethylsiloxane (PDMS)	30
2.4.2	Ecoflex	30
2.4.3	Eutectic Gallium Indium (EGaIn)	31
2.5	Artificial Intelligence (A.I.) in TENG	32
2.5.1	Introduction of A.I.	32
2.5.2	Machine Learning	33
2.5.3	Decision Tree (DT) and Random Forest (RF) Machine Learning Algorithms	33
2.5.4	Support Vector Machines (SVM) Learning Algorithm	34
2.5.5	Examples of A.I. in TENG	35
2.6	Conclusion	37
3	DESIGN AND DEVELOP OF A STRETCHABLE SELF-POWERED PRESSURE SENSOR BASED ON THE TRIBOELECTRIC PRINCIPLE	38
3.1	Overview	38
3.2	Design and Working Principle	38
3.3	Numerical Simulation and Fabrication of Sensor	41
3.4	Results and Discussion	42
3.4.1	Experiment Setup	42
3.4.2	Characterisation of Self-Powered Pressure Sensor	44
3.4.3	Application of Human-Machine Interface (HMI)	47
3.5	Summary	49
4	A PARAMETRIC STUDY OF A SPONGE-BASED TRIBOELECTRIC PRESSURE SENSOR	50
4.1	Overview	50
4.2	Design of SBTENG	51
4.2.1	Working Principle of SBTENG	52

4.2.2	Numerical Simulation	53
4.3	Fabrication of Sensor	53
4.4	Experimental Result and Discussion	56
4.4.1	Experiment Setup and Sensor Characterisation	56
4.4.2	Demonstration on Energy Harvesting Using SBTENG	58
4.5	Summary	58
5	STRETCHABLE, SELF-POWERED PRESSURE SENSOR FOR PNEUMATIC SOFT GRIPPER PICK-AND-PLACE SYSTEM	60
5.1	Overview	60
5.2	Design of Sensors and Soft Gripper Pick-and-Place System	60
5.3	Device Fabrication	62
5.4	Working Principle of Sensors	63
5.5	Numerical Simulation	65
5.6	Results and Discussions	66
5.6.1	Characterisation of Pressure Sensor	66
5.6.2	Characterisation of the Bend Sensor	69
5.7	The Functional Components of the Pick-and-Place System	71
5.8	Object Recognition	72
5.9	Summary	75
6	CONCLUSIONS AND FUTURE WORKS	76
6.1	Conclusions	76
6.2	Future Works	78
	REFERENCES	80
	PUBLICATIONS	87
	APPENDICES	88
	APPENDIX A: Ethical Approval for Research Project	88

LIST OF TABLES

Table		Page
2.1	Comparison of piezoelectric generator (PG) and triboelectric nanogenerator (TENG)	9
2.2	Triboelectric Series (Zou et al., 2019)	12
2.3	The comparison of the four operation methods of TENG	21
2.4	The comparison of the types of modification to improve TENG's performance	25
2.5	Comparison of the three classifiers in terms of overall accuracy and kappa values (Kavzoglu et al., 2020)	34

LIST OF FIGURES

Figure		Page
2.1	The charge generation mechanism of a TENG under external pressure. (Stage I) Initial state with no charge generation. (Stage II) potential difference between the triboelectric layers stays in equilibrium after the layers are in contact. (Stage III) External pressure is released from the surface, separating the two materials. (Stage IV) Potential differences between the triboelectric layers stay in equilibrium after the layers are released. (Stage V) External pressure is applied to the surface, and the two materials move closer.	11
2.2	The four fundamental modes of TENG. (a) Vertical contact-separation mode. (b) Contact-sliding mode. (c) Single-electrode mode. (d) Freestanding triboelectric-layer mode (Wang et al., 2016).	13
2.3	An example of a vertical contact separation mode TENG requires a spacer structure to create separation distance between the two triboelectric materials (Zhu et al., 2012).	14
2.4	Working principle of a lateral sliding mode TENG (Lin et al., 2013).	15
2.5	Working principle of a single electrode mode TENG (Wang et al., 2016).	18
2.6	Working principle of a freestanding triboelectric layer mode TENG (L. Zhang et al., 2020).	19
2.7	Comparison of performance on several surface-modified microstructures (pyramid, cube, line) on TENG layer (Fan et al., 2012).	23
2.8	Schematic illustration of a sponge structure based TENG. (a) Structure and fabrication process of the TENG. (b) FE-SEM images of the sponge-structured (Lee et al., 2014).	24
2.9	Electrical output performances of the film-based and sponge structure (0.5 μm) based TENG. (a) The output voltage, and (b) current density (Lee et al., 2014).	24

2.10	A schematic illustration describing contact electrification between a metal plate and a microstructured PDMS layer, resulting in larger pressure preforms greater contact electrification on the surfaces (Dharmasena et al., 2018).	28
2.11	An example of A.I. in TENG that function as a handwriting recognition system (W. Zhang et al., 2020).	35
2.12	Implementing A.I. in a glove-based TENG to identify gripping patterns when gripping different objects (Wen et al., 2020).	36
3.1	(a) Schematic illustration of the triboelectric-based soft pressure sensor. The inset is a photograph of the device. (b) Detailed operation principle of the soft pressure sensor. The periodic flow of water back-and-forth (i–ii–iii–iv–v–i) in the microchannel produces a triboelectric signal between the two electrodes.	39
3.2	(a) Simulation of electrical potential distribution in the water and PDMS triboelectric layers using COMSOL Multiphysics. (b) The fabrication process of the soft pressure sensor.	41
3.3	(a) Solidwork drawing of the experiment setup. (b) The experimental setup with the mechanical shaker. (c) The vibration configuration system.	43
3.4	(a)-(i) Temporal response of the triboelectric output from 1 Hz to 16 Hz under a constant input pressure of 50 kPa. (ii) Trendline of output voltage, V_{pp} at a different frequency. (b)-(i) Temporal response of the voltage output at different input pressure ranging from 50 kPa to 275 kPa under a fixed frequency at 7 Hz. (ii) Trendline of the output voltage, V_{pp} at different input pressure.	44
3.5	(a) Mechanical durability test under 2920 repeated cycles with input pressure of 50 kPa. (b) Stability test of the sensor after 1 hour, 2 hours, 168 hours (7 days) and 336 hours (14 days).	46
3.6	(a) The functional component of the HMI. (b)-(i) Output voltage against input pressure in controlling the LED light intensity (shown in the inset). (ii) Output voltage against input pressure in controlling	48

	the jumping height of a ninja character (shown in the inset).	
4.1	(a) Top view of the fabricated prototype. (b) Schematic illustration of the working mechanism of the SBTENG, (i) Original state, (ii) Pressing state, and (iii) Releasing state. (c) COMSOL simulation result of the non-porous structure and porous structure.	51
4.2	The fabrication processes of the SBTENG. (a) Solutions were added into a 3D-printed mold. (b) A syringe was used to stir and mix the components. (c) The cured prototype was carefully removed from the mold. (d) The prototype was immersed in deionized water to dissolve the NaCl particles. (e) The end product of the fabrication processes.	54
4.3	SEM images of cross-section of the conductive Ecoflex with (a) 0% concentration of NaCl particles, (b) 25% concentration of NaCl particles, (c) 45% concentration of NaCl particles, and (d) 65% concentration of NaCl particles.	55
4.4	(a) Study of the spring constant and elongation (under 5 N) with different NaCl concentration, ranging from 0% (non-porous), 25%, 45%, 65% to 70%. Inset of figure represents the experimental setup for measurement. (b) Study of the output voltage and current with different NaCl concentration (0%, 25%, 45% and 65%) under a constant 25 N compression force. Inset of figure represents the experimental setup for measurement. (c) Stability test of the sensor (65% NaCl concentration) after 1 hour, 2 hours, 168 hours (7 days) and 336 hours (14 days).	56
4.5	Demonstration of SBTENG to power up 5 LEDs by harvesting hand-tapping kinetic energy.	58
5.1	(a) Reaction of the fabricated bending sensor when the soft finger bends and unbends. (b) Schematic illustration of the triboelectric-based pneumatic soft gripper. (c) Fabricated pressure sensor which operates based on triboelectric mechanism. (d) Cartesian manipulator with the triboelectric-based pneumatic soft gripper attached. (e) Pick and place application. (f) AI object recognition application.	61

5.2	The simplified fabrication process of the sensors.	62
5.3	Detailed operation principle of the sensors from the (i) initial state to (ii) gripping an object state (Pressure sensor: The two triboelectric layers contact to each other as the sensor receives pressure input from the gripped object, bending sensor: two triboelectric layers separate due to the bending motion of soft finger) and finally to (iii) releasing an object state (Pressure sensor: The two triboelectric layers separate as in result of the removal of input pressure, bending sensor: two triboelectric layers contact due to the unbending of soft finger).	64
5.4	Simulation of the potential distribution in the sensors using COMSOL Multiphysics.	65
5.5	(a)-(i) Temporal response of the triboelectric output at different deflection on the pressure sensor ranging from 50 kPa to 275 kPa with an increment of 25 kPa. (a)-(ii) V_{pp} at different input pressure on the pressure sensor. (b) Mechanical durability test under 2200 seconds of continuous mechanical pressing with an input pressure and frequency of 150 kPa and 1 Hz. (c) Stability test of the sensor after 1 hour, 2 hours, 168 hours (7 days) and 336 hours (14 days).	67
5.6	The photograph of a single finger bending motion with a bending angle 0° to 60° (increment of 10°).	69
5.7	(a) The triboelectric output generated by the bending tip sensor has a bending angle of 0° to 60° . (b) The triboelectric output generated by the middle bending sensor with bending angle 0° to 60° . (c) Average voltage output of tip sensor in 336 hours (14 days).	70
5.8	The functional components of the pick-and-place system.	71
5.9	The result of gripping two sphere-shaped objects (diameter = 4 cm) with different surface hardness using a pressure sensor.	72
5.10	(a) The nine sensors (three pressure sensors and six bending angle sensors) are attached to the three fingers. (b) The confusion map of the object recognition result. (c) The voltage output corresponding to different gripping objects.	74

LIST OF ABBREVIATIONS

V_{pp}	peak-to-peak voltage
V_V	void volume
V_T	total volume
\emptyset	porosity
TENG	Triboelectric nanogenerator
PDMS	polydimethylsiloxane
HMI	human-machine interface
LED	light-emitting diode
DT	Decision Tree
RF	Random Forest
SVM	Support Vector Machine
PG	Piezoelectric generator
FEP	fluorinated ethylene propylene
AL	aluminium
EGaIn	Eutectic Gallium Indium
IoT	Internet of Things
A.I.	artificial intelligence
VR	virtual reality
AR	augmented reality
DI	deionized
PCB	printed circuit board
SBTENG	Sponge-based Triboelectric Energy Harvester
NaCl	Sodium chloride
SEM	Scanning electron microscope
ABS	acrylonitrile butadiene styrene
MCU	microcontroller unit
ADC	analog-digital converter

CHAPTER 1

INTRODUCTION

1.1 Background

Following Industry 4.0, the demand for pressure sensors has greatly surged up, including in the sector of wearable devices and soft robotics. However, traditional pressure sensors use batteries as power sources, requiring frequent replacement once they are depleted. Furthermore, improper battery disposal will create a severe environmental issue that could bring pollution. One alternative to solve the mentioned issue is to configure these sensors as a self-powered system (Wang, 2012) that can directly generate an electrical signal from the external stimuli without a battery.

Recently, the triboelectric nanogenerator (TENG) has received significant attention as a promising energy harvesting device to use as a self-powered pressure sensor because of its good sensitivity (Dharmasena et al., 2018) and sustainability (Lei et al., 2020). Although TENG has a wide selectivity range of constructing materials (Zou et al., 2019), most reported TENGs are usually developed using solid materials, which are not flexible and uncompatible with irregular and soft surfaces, including human skin and soft robotics' surfaces (Fan et al., 2017).

Studies have shown that the mechanical compliance of the TENG with the soft and irregular surfaces can be improved by constructing it with stretchable materials (Pan et al., 2020) such as Polydimethylsiloxane (PDMS) and Ecoflex. These silicon rubbers are stretchable (Qi et al., 2021) and have frequently paired up with various materials to design stretchable triboelectric wearable sensors (Pan et al., 2020). To explore pressure sensing on soft and irregular surfaces, we first design a pressure sensor using the microfluidic triboelectric principle for human pressure sensing. The pressure sensor consists of a water chamber and microchannel that are made with PDMS rubber material. When pressure is applied to the chamber, the liquid flows in the microchannel and transfers the negative ion to the rubber. This ion transportation makes the water a positive triboelectric layer, whereas the rubber becomes a negatively charged triboelectric layer (Nie et al., 2018). As a result, the polarity difference increases with the applied pressure, making it a promising candidate to detect slight and fast-changing fingertip pressure.

However, the output voltage saturates at high-pressure input, limiting the sensor from sensing more extensive pressure input such as hand tapping motion. Therefore, to expand the capability of the soft pressure sensor, it is necessary to improve its sensitivity. One approach of improving the sensor's output and sensitivity is to increase the contact surface area of the triboelectric materials. Integrating microstructure (Dharmasena and Silva, 2019) on the silicone rubber surface has dramatically increased the surface contact. More surface charges can be generated in contact electrification. Nonetheless, the continuous friction in the contact layers might create wear and tear. Embedding

micropores in the silicon layer could be an excellent alternative to reduce wear and tear. Furthermore, the microporous in the triboelectric layer can also help to trap more triboelectric charges (Ma et al., 2018). Inspired by the advantages of micropores, we designed our 2nd prototype in a micropores architecture.

Besides generating output voltage that can be used to power up LED light, we further integrate the pressure sensor in a soft robotic gripper. In the soft robotic gripper, the sensor compatibility with the soft structure is crucial to prevent damage to the gripped objects and improve the grasping performance (prevent falling of object). It can function as the end actuator of a pneumatically actuated soft gripper, gathering information from the gripped objects, such as their dimension and surface roughness, for pick-and-place and object recognition applications. With the integration of machine learning methods such as the support vector machine (SVM) learning approach, the triboelectric based sensor can be leveraged into a smart system. Our advanced triboelectric based pressure sensor has shown its great potential in ubiquitous computation, which indicates the possibility of building up a complex sensor network for future applications.

1.2 Problem Statements

Most reported triboelectric based pressure sensors are usually developed using solid materials, making them unsuitable to be applied on non-planar surfaces (Fan et al., 2017), such as human skin and soft robotics. Moreover, the solid-state feature has a high Young modulus which causes the material to crack

(Zou et al., 2019) at a low strain level. Therefore, they pose a high limitation in wearable devices and soft robotic applications. Using a Kirigami-based structure could improve the material elasticity by lowering the Young modulus and has been widely applied for sensor design (Park et al., 2019; Kong et al., 2021). Nonetheless, the sensor made of kirigami structure is not robust and is easily ruptured. Therefore, it is imperative to explore a softer material to develop a stretchable triboelectric-based pressure sensor for wearable devices and soft robotic applications.

1.3 Research Questions

This dissertation discusses the merits and performance of a self-powered, soft pressure sensor on soft and irregular surfaces. Therefore, the research questions of this project can be expressed as:

- (1) What self-powering mechanisms can be applied for pressure sensing on human skin and soft robotics?
- (2) What materials can be used in fabricating soft pressure sensors?
- (3) How can the characterisation of the fabricated sensors be conducted?
- (4) What are the applications that can be used to examine the performance of a soft pressure sensor?

1.4 Aim and Objectives

This dissertation designs soft and stretchable self-powered sensors based on the triboelectric principle. The triboelectric-based sensor conforms to soft and irregular surfaces, which can be applied to wearable devices and soft robotic applications. The specific objectives can be further expressed as:

- (1) To explore self-powering mechanisms based on the contact electrification principle for pressure sensing on human skin and soft robotics.
- (2) To fabricate and characterize soft, self-powered pressure sensors for their frequency-dependent behaviors.
- (3) To examine the performance of the fabricated soft pressure sensors for both wearable devices and soft robotic applications.

1.5 Dissertation Outline

This dissertation is organized into six chapters. Each chapter will be covered as follows:

Chapter 1 discusses the background of self-powered sensors and elaborates on the detail of triboelectrification. Conventional triboelectric layers are made of solid-state material, which raised concerns in designing a sensor that complies with soft and irregular surfaces. This chapter elaborates on the

problem associated with the solid-state triboelectric sensor and proposes a solution by constructing it with soft and stretchable materials.

Studies have shown that the mechanical compliance of the TENG with the irregular surface can be improved by constructing it with stretchable material (Pan et al., 2020), such as silicone rubber, or formless material such as water. Thus,

Chapter 2 reviews the basic theory in TENG sensor design and the comparison with another self-powering mechanism. The external and internal parameters which could affect the TENG performance are highlighted in this chapter. Lastly, artificial intelligence (AI) application using TENG sensors is discussed.

Chapter 3 presents our first sensor using a microfluidic approach. The design is supported by the working principle, fabrication processes, numerical simulation, and experimental results. The end of the chapter demonstrates the wearable pressure sensor for human-machine interaction (HMI) application for controlling the light intensity and gaming character.

Chapter 4 proposed an improvement method by replacing the water with a eutectic gallium-indium (EGaIn). The EGaIn is embedded into the PDMS material and constructed in a sponge-like structure. This improvement could help eliminates the pressure sensor's dependency on the liquid behavior and increase the generated output voltage. The relationship between the porosity and

the output power was studied. This chapter also demonstrated a proof-of-concept experiment to power up LEDs using the improved structure.

Chapter 5 integrated the improved version of the microporous sensor into a pneumatically actuated soft robotic gripper for pick and place operations. The working principle, fabrication processes, numerical simulation, and experimental results were vividly elaborated. The microporous TENG sensor was then programmed with an AI algorithm to perform object recognition.

The future works and the improvement method were proposed in Chapter 6.

CHAPTER 2

LITERATURE REVIEW

2.1 Self-Powered Technology

Self-powered technology is an approach that harvests energy from the environment for wearable electronics to operate without an external power source. Most conventional sensing systems require maintenance, such as replacing batteries. The process of replacing the batteries is an inconvenience for biomedical applications, especially implantable devices. It may cause the user infection (Hasan et al., 2021). On top of that, the non-stretchable form of the battery may also limit the sensor's functionality. Although integrating a wireless power transfer module (Chee et al., 2016; Chee et al., 2015) could be considered a promising solution, a short transmission distance between the transmitter and the receiver can limit the sensor's mobility.

Researchers have utilized random energy (Z. L. Wang, 2012) in recent decades as vibration-based ambient mechanical energy from human activity as the solution for the sustainable energy supply of wearable electronics. The most common approaches for harvesting vibration-based ambient mechanical energy are piezoelectric generators (PGs) and triboelectric nanogenerators (TENGs).

2.1.1 Piezoelectric Generators (PGs) Vs. Triboelectric Nanogenerators (TENGs)

PGs operate based on the polarization of the dipole moment from piezoelectric materials. They are made of ceramic materials, such as lead zirconate titanate (Lin and Giurgiutiu, 2006), with a brittle structure and low output power (Lee et al., 2012). The triboelectric nanogenerators, on the other hand, works based on the coupling of contact electrification and electrostatic induction between two dissimilar triboelectric materials. This mechanism leads to electron flow in the external circuits (Wu et al., 2019). The TENG provides high material selection flexibility (Wu et al., 2019) and can construct a stretchable platform with simple fabrication methods. Besides the mentioned advantages, TENG generates higher output (around twice the power density) than the PG (Ahmed et al., 2020) based on power generation per unit mass metric. The same study also pointed out that the TENG could produce electrical output in a low-frequency region (as low as 0.2 Hz), outranked the PG, which could only generate electrical output at 1 Hz and above. The comparison of the generators has been summarised in Table 2.1.

Types	Materials	Advantages	Disadvantages	References
Piezoelectric generator (PG)	- Lead zirconate titanate - Narrow material selection	- Generates higher current output than TENG	- Brittle structure - Limited to an operating frequency above 1 Hz - Generates lower voltage	(Lin and Giurgiutiu, 2006) (Ahmed et al., 2020)

			output than TENG	
Triboelectric nanogenerator (TENG)	<ul style="list-style-type: none"> - Metals, nylon, silicone rubbers, polymers etc. - Wide material selection 	<ul style="list-style-type: none"> - Can be constructed with soft materials - Generates higher voltage output than the PG 	- Generates lower current output than PG	<p>(Wu et al., 2019)</p> <p>(Ahmed et al., 2020)</p>

Table 2.1: Comparison of piezoelectric generator (PG) and triboelectric nanogenerator (TENG)

2.2 Introduction of Triboelectric Nanogenerators (TENGs)

This section elaborates on the working principle of TENG, the constructed materials, and four operating modes.

2.2.1 Triboelectric Effect

Figure 2.1 shows an example of charge generation under external pressure. A simple TENG design consists of two triboelectric materials. The two materials will be deposited with electrodes on their surfaces and connected to an external load (shown as the black colour block in Figure 2.1) for the free electrons to flow from one material to another. Hence, a large contact area between two triboelectric materials allows more electrons to be transferred (Dharmasena and Silva, 2019).

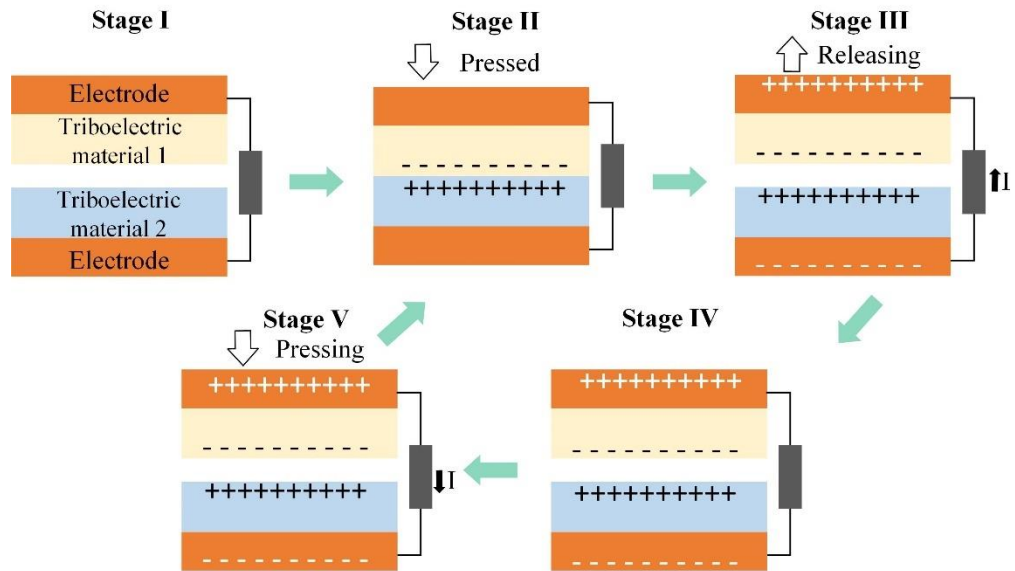


Figure 2.1: The charge generation mechanism of a TENG under external pressure. (Stage I) Initial state with no charge generation. (Stage II) potential difference between the triboelectric layers stays in equilibrium after the layers are in contact. (Stage III) External pressure is released from the surface, separating the two materials. (Stage IV) Potential differences between the triboelectric layers stay in equilibrium after the layers are released. (Stage V) External pressure is applied to the surface, and the two materials move closer.

Figure 2.1 (Stage I) shows that the two materials are maintained at a fixed distance. Both materials remain in a neutral state (no charge transportation occurs). At an applied external pressing pressure, both triboelectric materials contacts. The surface charge transfers at the contact area of the two materials due to the triboelectrification effect. The charge transfers are only constricted on the contacted surface, with no difference in electric potential on the connected electrodes (Figure 2.1 (Stage II)). When the external pressing pressure is released, the two triboelectric materials separate. A potential difference is generated between the connected electrodes due to the disengagement of the triboelectric charges. This leads to an induction of electrical current when the electron flows from the top electrode to the bottom electrode (Figure 2.1 (Stage III)). The potential difference between the

connected electrodes increases with the separation until it reaches a maximum value. In this stage, the potential difference backs to equilibrium when the two materials are entirely separated (Figure 2.1 (Stage IV)).

When external pressing pressure is applied to the surface, the equilibrium state diminishes due to the reduction of the separation distance between the two materials. The top electrode possesses a larger electric potential to drive the electrons from the bottom electrode to the top electrode and induces a current in the opposite direction (Figure 2.1 (Stage V)). The potential difference between the connected electrodes returns to an equilibrium state when the two materials are entirely contacted again (Figure 2.1 (Stage II)).

2.2.2 Triboelectric Series

	Polyurethane foam	(continued)	
	Etylcellulose	Polyester (Dacron)	
	Sorbothane	Polyisobutylene	
	Polyamide 6-6	Polyurethane flexible sponge	
	Hair, oily skin	Polyethylene Terephthalate (PET)	
	Wool, Knitted	Polyvinyl butyral	
	Silk, woven	Polychlorobutadiene	
	Aluminum	Natural rubber	
	Paper	Polyacrilonitrile	
	Cotton, woven	Polystyrene	
	Steel	Polyimide	
	Wood	Neoprene	
	Hard rubber	Polyehylene	
	Nickel, copper	Polypropylene	
	Sulfur	Polyimide (Kapton)	
	Brass, silver	Polyvinyl chloride (PVC)	
	Acetate, Rayon	Latex (natural) rubber	
	Polymethyl methacrylate (Lucite)	Santoprene rubber	
	Polyvinyl alcohol	Polydimethylsiloxane (PDMS)	
	(continued)	Polytetrafluoroethylene (Teflon)	

Table 2.2: Triboelectric Series (Zou et al., 2019).

The tendency to gain or lose electrons of the triboelectric layer is based on the material's natural property (Zou et al., 2019). Table 2.2 shows some examples of the material in the triboelectric series. The left column (more electropositive) in Table 2.2 shows that the materials have a better tendency to lose electrons than those in the right column (more electronegative). Hence, materials that are more electronegative attract electrons from the more electropositive materials (left column). This triboelectric series serves as a reference in selecting the materials for TENG sensor design.

2.2.3 Fundamental Operation Modes of TENG

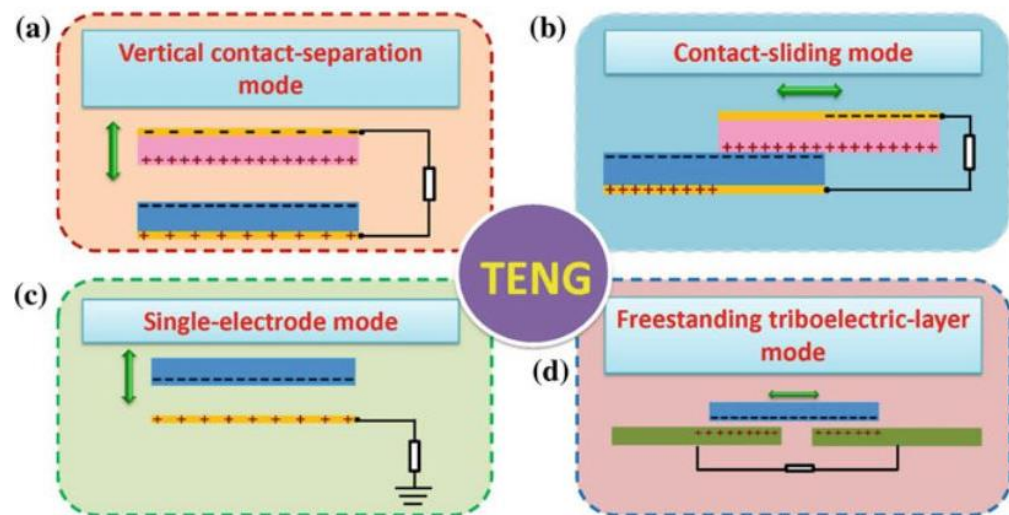


Figure 2.2: The four fundamental modes of TENG. (a) Vertical contact-separation mode. (b) Contact-sliding mode. (c) Single-electrode mode. (d) Freestanding triboelectric-layer mode (Wang et al., 2016).

There are four operation modes for the TENG sensor. Each of these modes utilizes its structure to achieve the contact and separation of the triboelectric materials. The four operating modes are illustrated in Figure 2.2.

2.2.3.1 Vertical Contact Separation Mode

The vertical contact separation (shown in Figure 2.2 (a)) is the most used mode in TENG design. The two dissimilar materials are separated with a small gap in this mode. When external pressure is applied to one of the surfaces, the separation gap is filled and making the two materials in close contact. When the external pressure is removed, the two materials separate and cause a potential drop. The charge transfer occurs electrically when an external load connects the two materials.

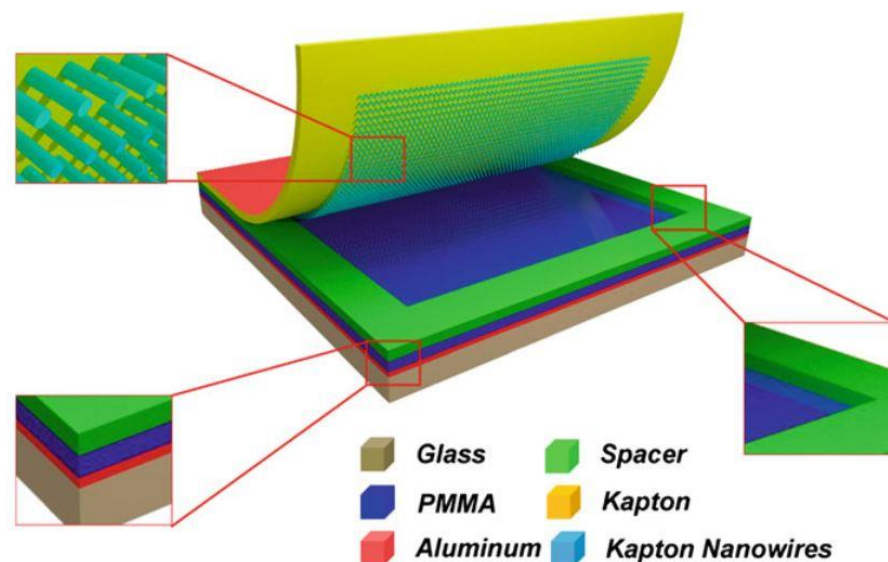


Figure 2.3: An example of a vertical contact separation mode TENG requires a spacer structure to create separation distance between the two triboelectric materials (Zhu et al., 2012).

The separation gap between the structure plays an essential role in triboelectrification as a larger separation distance will induce a larger potential drop. Hence, this mode requires a “spacer” to create separation between the two materials, such as the example depicted in Figure 2.3.

2.2.3.2 Lateral-Sliding Mode

The lateral-sliding mode TENG works based on the sliding of the triboelectric materials. Unlike the vertical contact-separation mode, the contact and separation of the two triboelectric materials are created in a horizontal sliding motion instead of a vertical direction. An illustration of the lateral sliding mode is presented in Figure 2.4.

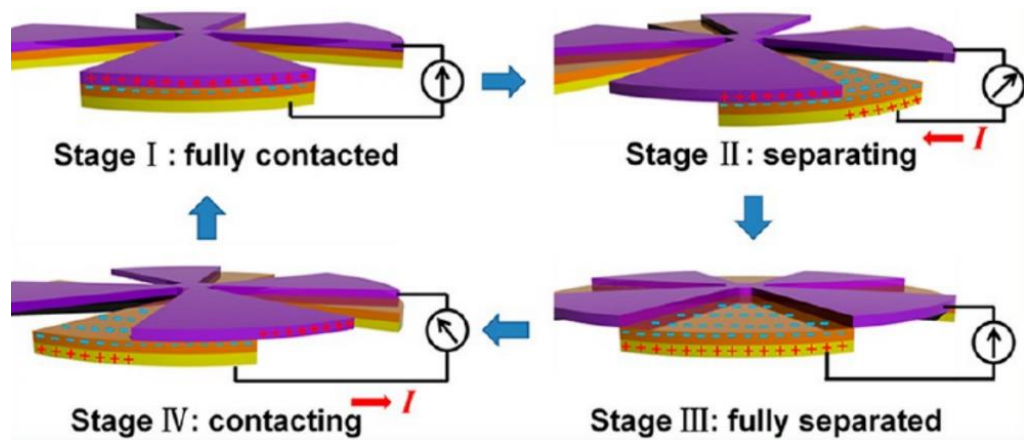


Figure 2.4: Working principle of a lateral sliding mode TENG (Lin et al., 2013).

Figure 2.4 shows that the Kapton layer (orange layer) attracts electrons from the aluminium layer (purple layer). The Kapton and aluminium layers become negatively and positively charged during the first contact (Stage I). Since the aluminium is conductive, the aluminium layer simultaneously acts as the triboelectric material and electrode. This configuration can reduce the need for another electrode. In Stage II, the two materials began to separate horizontally. During the separation of the aluminium and Kapton layers, a potential difference is generated between the connected electrode (yellow layer) and aluminium layer due to the disengagement of the triboelectric charges.

Therefore, an electrical current is induced and flows from the aluminium layer to the bottom electrode.

When the two materials are fully separated, as shown in Stage III, the potential difference increases until it reaches a maximum value where the charges are no longer in transfer. Therefore, the potential difference returns to the equilibrium state. Lastly, in Stage IV, the aluminium layer slides back to the original location and starts a new contacting motion with the Kapton layer. Hence, the extra electrons flow through the connector and generate an electrical signal in the opposite direction. This design is often used in strain sensing, and it does not require an air gap as the separation distance. However, the friction on the sliding surfaces may create wear and tear to the materials, reducing their durability significantly (Tang et al., 2019).

2.2.3.3 Single Electrode Mode

The single electrode mode is the simplest operation mode in TENG designs (Zhang et al., 2016; Ankanahalli Shankaregowda et al., 2019; Mule et al., 2019). Same as other modes, it requires two triboelectric materials. However, only one electrode is needed as another electrode layer is grounded. An example of a conductor-dielectric single electrode mode TENG which operates based on contact electrification and electrostatic induction is shown in Figure 2.5. This design uses two triboelectric materials, fluorinated ethylene propylene (FEP) and aluminium (Al).

Aluminium (conductivity = 3.77×10^7 S/m) can simultaneously act as triboelectric material and the electrode due to its conductive nature. Besides its conductive nature, aluminium is also a conductor with a larger tendency to lose electrons than other conductors such as brass, silver, and steel, as shown in the triboelectric series (Table 2.2). Therefore, it is a good conductor to be paired with materials with a stronger ability to attract electrons, such as FEP. As shown in Figure 2.5, the aluminium works as one of the triboelectric layers and the primary electrode. The copper works as the reference electrode that can provide or receive electrons from the aluminium to equalize the electrical potential difference on the aluminium layer. According to the triboelectric series, aluminium tends to lose electrons. Therefore, the electrons are attracted from the aluminium layer to FEP when the two dissimilar materials contact (Figure 2.5 (a)). Thus, the FEP and aluminium layers were negatively and positively charged, respectively.

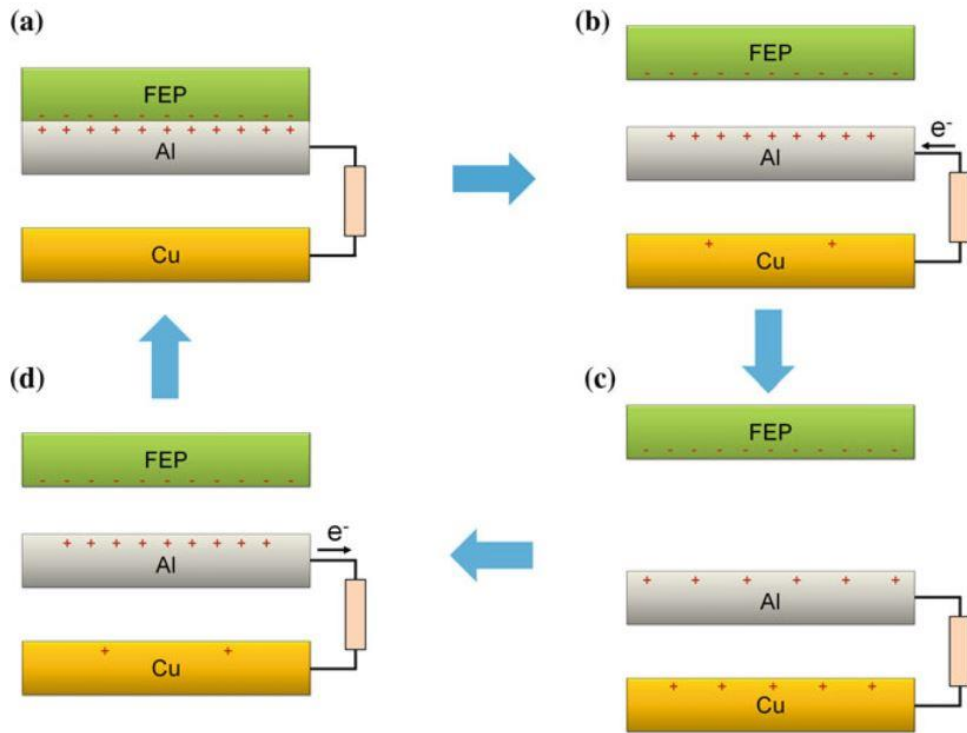


Figure 2.5: Working principle of a single electrode mode TENG (Wang et al., 2016).

When the FEP is no longer contacted with the aluminium layer (Figure 5. (b)), the aluminium layer will stay in positive charge and electrons will be transferred from the copper (reference electrode) to the aluminium layer (primary electrode) to equalize the potential difference on the aluminium layer. Oppositely, when the FEP layer is contacting back to the aluminium layer (Figure 2.5. (c)-(d)), the charge will be transferred in a reverse manner. This configuration can be used to harvest energy from a freely moving object. Hence, mobility is its most significant advantage. However, the single electrode mode is commonly known to degrade output performance after long operation hours due to the electrostatic shield effect of the primary electrode (Niu et al., 2014). Moreover, the sensing performance may vary based on different materials' affinity.

2.2.3.4 Freestanding Triboelectric Layer Mode

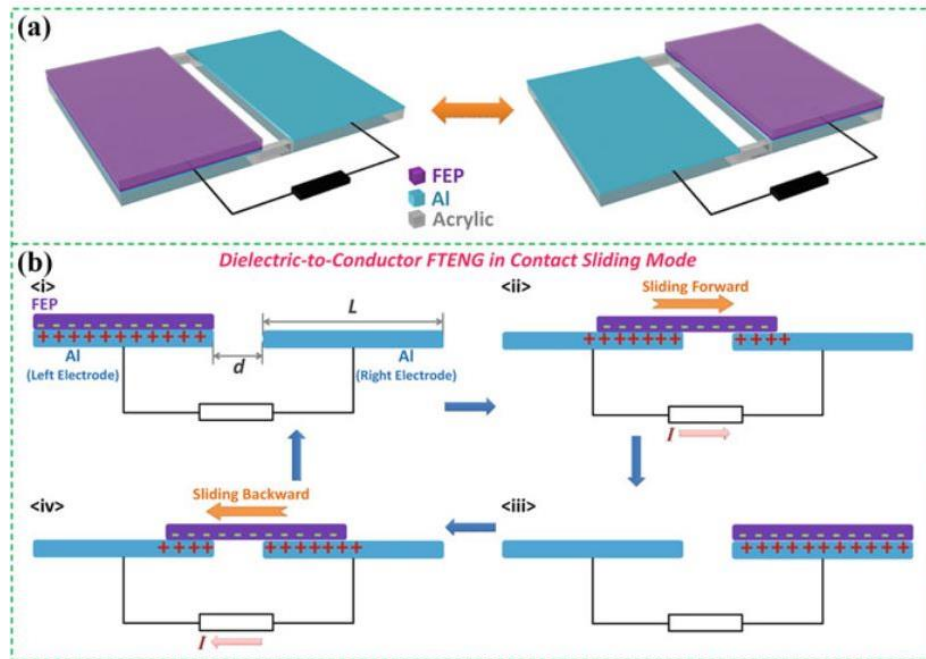


Figure 2.6: Working principle of a freestanding triboelectric layer mode TENG (L. Zhang et al., 2020).

The final triboelectric operation mode is the freestanding triboelectric layer mode. The example in Figure 2.6 (L. Zhang et al., 2020) consists of one freestanding triboelectric layer (FEP in this example), which can slide in between the stationary electrodes (aluminium in this example) when an external force is applied. The contact area of the FEP layer and the two aluminium layers increases/decreases when it slides (Figure 2.6 (b) (ii)-(iv)). Thus, it enables periodic changing of induced potential difference between the connected electrodes. The extra electrons flow from one electrode to another to equalize the potential difference. Similar to the lateral sliding mode, the freestanding triboelectric layer mode can harvest energy from sliding motions (Toyabur Rahman et al., 2020; L. Zhang et al., 2020; Wang et al., 2014). However, the sliding movement may create damage to the solid materials. One solution is

integrating the freestanding triboelectric layer mode TENG with the microfluidic technique (Shi et al., 2016).

2.2.3.5 Comparison of the four operation methods of TENG

Vertical contact separation and single electrode modes are commonly used to design pressure sensors. Both modes detect pressure change based on the change in separation distance. On the other hand, lateral sliding and freestanding modes are suitable for strain sensing as they operate based on the horizontal sliding motion to create a change in the contact area of the materials. However, the friction on the sliding surfaces may create wear and tear to the materials, reducing their durability significantly. To solve the issue, the freestanding mode is utilised with the microfluidic technique (Shi et al., 2016) to reduce contact friction. Table 2.3 represents the comparison of the four methods. We designed our first sensor in spiral shape microfluidic channel. It operates in a freestanding mode that is more space-efficient than the previous literature (Shi et al., 2016). For our second sensor design, vertical contact separation mode was used for better compliance with a soft robotic gripper.

Type	Working principle	Advantages	Disadvantages	References
Vertical Contact Separation Mode	- Based on the vertical separation distance between materials	- Suitable for pressure sensing	- Requires macro-scale air gap that would enlarge the size of the prototype	(Zhu et al., 2012).
Lateral-Sliding Mode	- Based on horizontal sliding of the	- Suitable for strain sensing	- Friction on the sliding surfaces may create wear	(Lin et al., 2013)

	triboelectric materials		and tear to the materials	(Tang et al., 2019).
Single Electrode Mode	Based on the vertical separation distance between a static and mobile layer.	<ul style="list-style-type: none"> - Simplest structure - High mobility - Suitable for pressure sensing 	<ul style="list-style-type: none"> - Sensing performance may vary based on different materials' affinity 	<ul style="list-style-type: none"> (Zhang et al., 2016) (Niu et al., 2014)
Freestanding Triboelectric Layer Mode	- Based on horizontal sliding of the triboelectric materials	<ul style="list-style-type: none"> - Suitable for strain sensing - Can be integrated with microfluidics design 	<ul style="list-style-type: none"> - Friction on the sliding surfaces may create wear and tear to the materials 	<ul style="list-style-type: none"> (L. Zhang et al., 2020) (Shi et al., 2016).

Table 2.3: The comparison of the four operation methods of TENG.

2.3 Modification to improve TENG's performance

The improvement of TENG's performance is one of the significant efforts to expand its capabilities to cater to different applications. Hence, in this section, the methods to improve TENG's performance include physical modification of the TENG layers, material selection, input motion (operating frequency, movement amplitude, and input pressure), and environmental parameters that influence the performance of the TENGs are discussed.

2.3.1 Physical Modification of TENG Layers

As mentioned in Section 2.2.1, a large contact area between two triboelectric materials generates larger output (Dharmasena and Silva, 2019). However, this mode is not suitable for miniaturization. Physical modification, such as introducing microstructures on the surface of the TENG layer, has been proven to be an effective method in enhancing the contact area of the triboelectric layers. Utilising the same space helps improve the charge generation from contact electrification (Song et al., 2018; Zhao et al., 2016; Wang et al., 2015). Fan et al. compared the effectiveness of using several surface modifications triboelectric layers with a flat PDMS film.

Figure 2.7 shows that the pyramid microstructure best enhances the generated output (about 5–6 times improvement compared with the unstructured films). The pyramid microstructure has an excellent geometric and a sharp tip, which is advantageous in enlarging the friction area (Fan et al., 2012). Thus, the efficiency of the power generation process increased. The cube structure ranked second after the pyramid structure, and lastly, the line structure, proven from their voltage and current outputs.

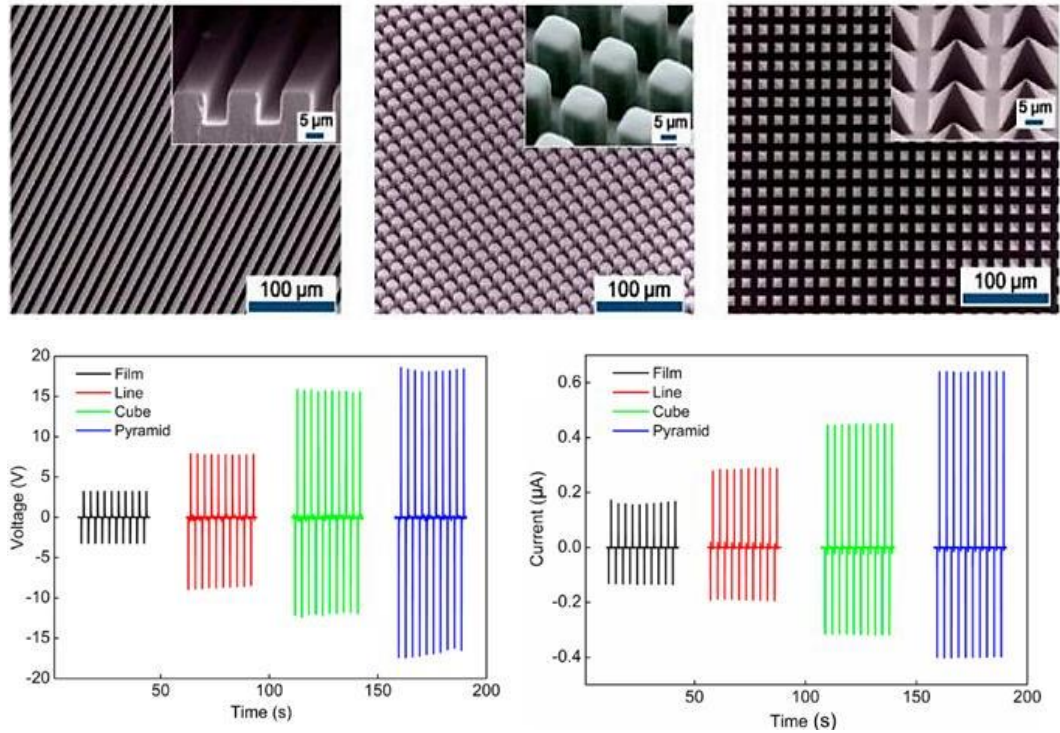


Figure 2.7: Comparison of performance on several surface-modified microstructures (pyramid, cube, line) on TENG layer (Fan et al., 2012).

Other than the mentioned structures, nanoparticles and nanowires have also been reported to improve the output performance of TENG (Bai et al., 2013; Chen et al., 2013). The integration of these structures has largely increased the friction on the contacted surfaces, which has shown great improvement (up to 4 times) in the generated output (Zheng et al., 2014). However, these surface-type modifications are prone to wear and tear due to the contact friction between the triboelectric layers. Another approach that could address the constraint is introducing microporous (pore's diameter $\sim 0.5 \mu\text{m}$) in the triboelectric layers (Lee et al., 2014), as shown in Figure 2.8. Figure 2.8 elucidates that the triboelectric layer can form a sponge-like structure using the sacrificial method.

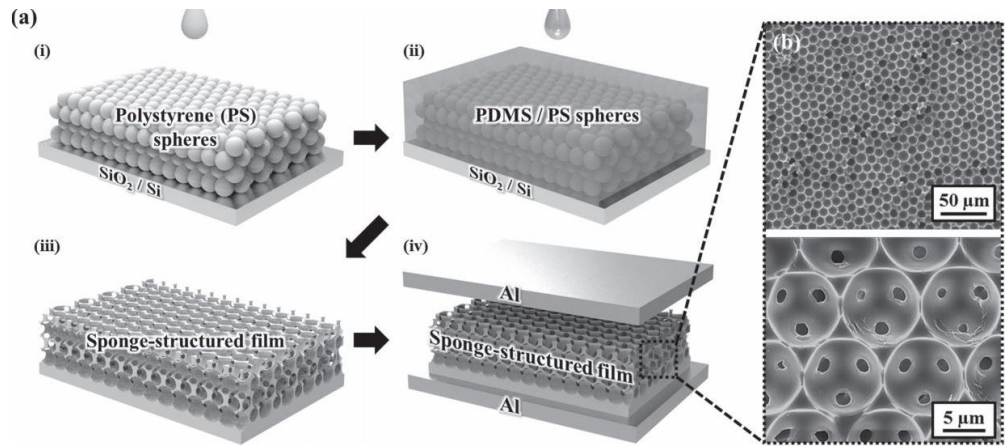


Figure 2.8: Schematic illustration of a sponge structure based TENG. (a) Structure and fabrication process of the TENG. (b) FE-SEM images of the sponge-structured (Lee et al., 2014).

Figure 2.9 shows the sponge-based structure has an increase factor of 3 times in the voltage output and five times in the current output under a cycled compressive force of 90 N with an operating frequency of 10 Hz. Besides enhancing the contacted area, the microporous trap more charge in its pores, which further improves the generated output (Sahu et al., 2021). In short, the introduction of microporous within the triboelectric layer increases the contacted effective area and avoids damage from the friction. Hence, it has larger durability compared to surface-type modifications.

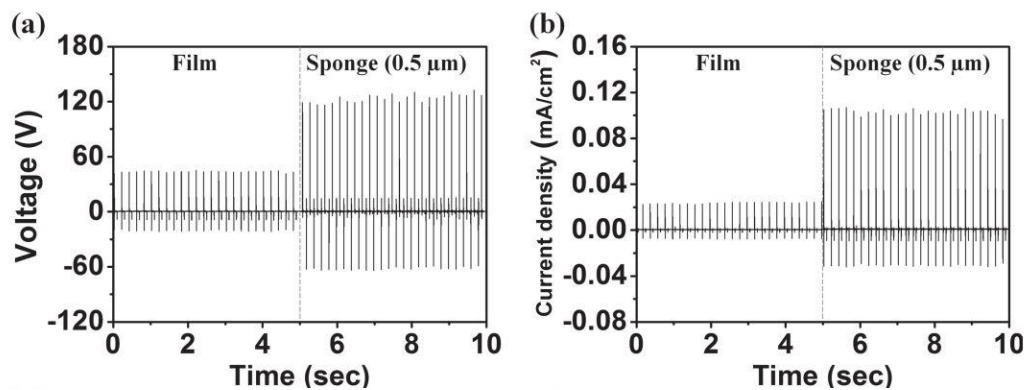


Figure 2.9: Electrical output performances of the film-based and sponge structure (0.5 μm) based TENG. (a) The output voltage, and (b) current density (Lee et al., 2014).

Types of microstructures	Improvement made to unstructured film (in voltage)	Advantages	Disadvantages	References
Surface integrated line structure	- 2.5 times greater	- Easier to be modified	- Prone to wear and tear due to the contact friction	(Fan et al., 2012)
Surface integrated cube structure	- 3.5 times greater	- Easier to be modified	- Prone to wear and tear due to the contact friction	(Fan et al., 2012)
Surface integrated pyramid structure	- 5 times greater	- Best in enhancing output performance - Easier to be modified	- Prone to wear and tear due to the contact friction	(Fan et al., 2012)
Surface integrated nanowires	- 4 times greater	- Easier to be modified	- Prone to wear and tear due to the contact friction	(Bai et al., 2013) (Chen et al., 2013)
Internal integrated porous structure	- 3 times greater	- Best in durability - Does not prone to wear and tear due to the contact friction	- Internal modification is more difficult	(Lee et al., 2014)

Table 2.4: The comparison of the types of modification to improve TENG's performance.

The comparison of the methods for improving the performance of TENG is summarised in Table 2.4. Table 2.4 shows that surface modification is an effective method in enhancing the contact area of the triboelectric layers, with contributes to an increase factor of 2.5 to 5 times to the output voltage.

However, these surface type modifications are prone to wear and tear due to the contact friction. Therefore, our design introduces a porous structure into an elastomer TENG for better durability than the surface-type modifications mentioned in Table 2.4.

2.3.2 Material Selection for TENG Layers

TENG can be fabricated from various materials, including metals, polymers, inorganic materials, and liquids. The performance of the TENG is strongly related to the materials that are ranked in the triboelectric series. The further the two materials are ranked in the triboelectric series, the larger difference in their tendency to gain or lose electrons (Lee et al., 2017). Thus, they produce larger potential differences during triboelectrification.

It is worth mentioning that the triboelectric layer made of metal discharged efficiently, even before they are separated, attributed to the high electrons mobility. This issue can be solved by replacing the triboelectric layer with an insulator, which helps in retaining the triboelectric charges on the metal surface. Triboelectricity between the metal-insulator and insulator-insulator materials is more stable and preferable in energy harvesting (Wang, 2014).

2.3.3 Operating Parameters: Frequency, Movement Amplitude, and Input Pressure

The parameters that affect the triboelectric output are discussed in this subsection, such as the operating frequency (motion rate), the movement

amplitude (separation distance) between the triboelectric layers, and the input pressure that deforms the layers when the two layers are in contact.

The power generation of the TENG increases with the operating frequency as it enhances the movement speed of two triboelectric layers. Thus, the charge transfer rate increases and directly improves the output power (Dharmasena et al., 2018; Yang and Daoud, 2018). Therefore, it is advantageous to operate the TENG sensor at a high rate to achieve larger outputs, mainly when it is meant for energy harvesting applications.

The movement amplitude or separation distance considerably influences the TENG's performance. The increase in separation distance enlarges the gap between the triboelectric layers and induces a larger potential difference (Wang et al., 2016). Therefore, the magnitude of the output voltage and current increase.

An experiment has been conducted by (Dharmasena et al., 2018) on a TENG sensor with pyramid-shaped microstructures integrated to study the pressure-voltage relationship. The result showed that the deformation level of the triboelectric at an applied pressure affects the output voltage. As shown in Figure 2.10, larger input pressure contributes to larger deformation on the microstructures, making the two layers have better conformal contact. Hence, the contact surface area increases and provides greater contact electrification on the surfaces. When they are brought into contact, the input pressure that deforms the layers is crucial in increasing contact electrification, primarily when the surfaces are structured.

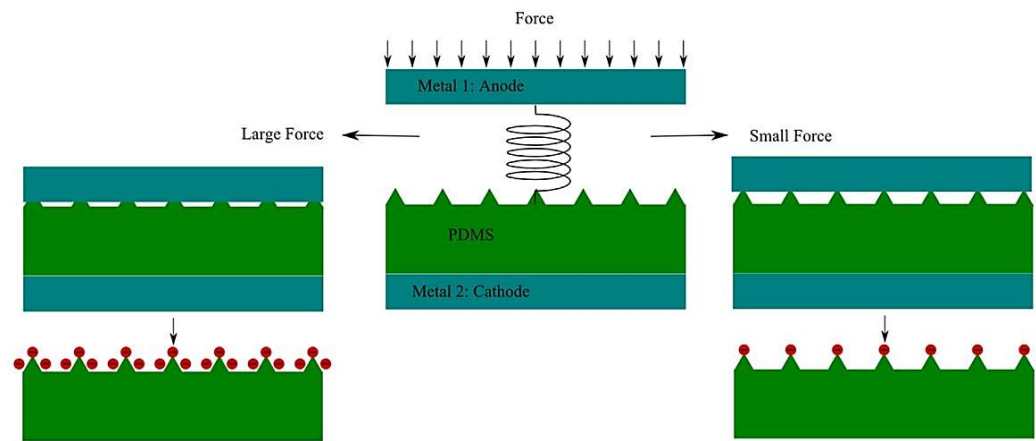


Figure 2.10: A schematic illustration describing contact electrification between a metal plate and a microstructured PDMS layer, resulting in larger pressure preforms greater contact electrification on the surfaces (Dharmasena et al., 2018).

2.3.4 Environment Parameters

Besides the mentioned operating parameters, the triboelectric output is also affected by environmental parameters such as temperature, humidity, and atmospheric pressure (Diaz and Felix-Navarro, 2004). These parameters shall be taken into consideration for TENG sensor design.

Xu et al. (Xu et al., 2018) reported that the TENG outputs, including charge, voltage, and current reduced when the environmental temperature increased from 293 K to 473 K. The TENG output rose at the beginning of the temperatures (77 K–260 K) as the temperature softened the TENG surfaces and caused greater conformal contact on both layers. Nonetheless, further increases in the temperature cause the electrons to discharge and reduce the triboelectric charge density.

The triboelectric output depends on humidity and the surface's wettability (Xu et al., 2018). The hydrophilic surface attracts moisture, making the contact area lesser, and generating weaker triboelectric charge density. Nonetheless, some literature reported it is necessary for maintaining considerable humidity conditions for polymers-based TENG (Baytekin et al., 2011). It helps to keep a water layer on the polymer surface, where charges can be stabilized (Baytekin et al., 2011). Therefore, a balance in the humidity level is required to achieve optimum sensor performance.

One of the significant limitations on the output performance of the TENG sensor is the air breakdown effect. It limits the TENG sensor's ability to retain its charge density when operated in a vertical-contact-separation mode (Zi et al., 2017). A study reported that the performance of the TENG sensor improved in a high vacuum environment as it eliminates the air breakdown effect, which often occurs under atmospheric pressure conditions (Diaz and Felix-Navarro, 2004). In addition, the high vacuum environment also eliminates air moisture.

2.4 Stretchable Materials in TENG Sensor

Stretchable materials are the fundamental elements to develop a stretchable TENG. These materials allow the devices to withstand deformations without cracking and comply with human skin. Thus, they appear as a promising candidate for developing a wearable TENG for healthcare monitoring, human motion detection, and soft robotic application. This section discusses the commonly used stretchable materials in TENG fabrication.

2.4.1 Polydimethylsiloxane (PDMS)

Polydimethylsiloxane (PDMS) is a non-toxic, flexible, bio-compatible, and transparent silicone elastomer that has been widely used in developing stretchable TENG (Qi et al., 2021; Li et al., 2019; Ko et al., 2014). The elastic modulus of the PDMS can be tuned in the range of 1.32 - 2.97 MPa based on the mixing ratio between the monomer and the curing agent. Referring to the triboelectric series (presented in Section 2.2.2), PDMS is one of the materials with the best tendency to attract electrons, making it an excellent material to be paired with materials that have a greater tendency to lose electrons such as human skin and copper. Moreover, it is an easily molded material as it remains in a liquid form before it cures, which is beneficial in forming different microstructures patterns on the surface (Gong et al., 2017; Song et al., 2018).

2.4.2 Ecoflex

Similar to the PDMS, another silicon rubber, Ecoflex (Smooth-on-Inc, USA) is also a non-toxic and biocompatible elastomer. Compared to PDMS, Ecoflex has a lower Young's modulus of 125 kPa, which is nearer to the human skin's value at 420-850 kPa (Lu et al., 2012, Park et al., 2010). Due to the similar nature to PDMS, Ecoflex is also an excellent material to be paired with materials with a greater tendency to lose electrons (refer to triboelectric series in Section 2.2.2). However, Ecoflex is better at withstanding large pressure input as it is more environmentally stable, which does not have an ageing effect (Deuschle et al., 2010). After multiple stretching, it also shows no distortion and will

rebound to its original form immediately, making it a better material for a pressure-triggered TENG sensor (Liu et al., 2019; Nayak et al., 2019).

2.4.3 Eutectic Gallium Indium (EGaIn)

Eutectic gallium indium (EGaIn), with a composite of 68.5% Ga, 21.5% In, 10% Sn by weight, is a conductive liquid metal that has a similar conductivity (3.4×10^4 S/cm) to mercury (1.04×10^4 S/cm). However, mercury has high toxicity (Rice et al., 2014), and its high surface energy (>400 mN m⁻¹) makes it harder to be patterned into desired shapes. EGaIn, on the other hand, has lower toxicity and has been widely reported as stretchable electrodes for TENGs applications (Yang et al., 2018; Tang et al., 2015). This might be attributed to its easily transformed feature by external forces without losing its conductivity. Y. Yang et al. demonstrated a great combination of Ecoflex and EGaIn in developing stretchable pressure and strain sensor with high durability (Yang et al., 2018). However, the melting point of the EGaIn (30 °C) is very close to room temperature, making it stay in a liquid form. Thus, it requires good sealing to prevent the leaking of the EGaIn when pressure is applied to the TENG sensor. A promising solution to address the leaking issue is by embedding the EGaIn into Ecoflex (Park et al., 2021) before it cures to create stretchable electrodes. This method eliminates non-stretchable solid electrodes and allows the stretchable TENG to have better conformal contact with irregular surfaces.

2.5 Artificial Intelligence (A.I.) in TENG

There will be over 30 billion sensors connected to the internet of things (IoT) (Yang, 2018) and artificial intelligence applications in the future. Hence, the demand for the high amount of batteries for sensors operation will be a challenge for A.I. applications as it is space and power-consuming. Due to its simple structure, TENG is one of the most accessible self-powered mechanisms for artificial intelligence applications. This section introduces artificial intelligence basics and provides examples of A.I. in TENG application.

2.5.1 Introduction of A.I.

Artificial intelligence (A.I.) is an intelligent system that uses data and analysis to mimic brain cognition and solve complex problems without the involvement of humans. A.I. programming focuses on three cognitive skills: learning, reasoning, and self-correction (Haleem et al., 2020). Generally, A.I. systems work by analysing numerous training data to determine their correlations and predict the next states. A.I. systems can be distinguished into weak, strong, and super A.I.s (Sergievskaa, 2020; Andrejevic and Selwyn, 2020; Okuda and Shoda, 2018).

Weak A.I. or narrow A.I. is the most common and only type of A.I. capable of performing specific tasks instead of fully cognitive abilities like the human brain. Examples of weak A.I. include virtual assistance, chatbots (Okuda and Shoda, 2018), facial recognition (Andrejevic and Selwyn, 2020), and autonomous vehicles' vision (Ma et al., 2020). Strong or general A.I. exhibits

intelligence level as a human. Theoretically, a strong A.I. can think and respond to different situations like a human (Hildt, 2019). Super A.I. can surpass human intelligence and ability in every possible way (Sergievskii, 2020).

2.5.2 Machine Learning

Unlike automation, A.I. system does not require pre-programmed. Instead, it uses machine learning algorithms such as the decision tree (DT), random forest (RF), and support vector machines (SVM) to learn from massive historical data to make predictions without being programmed.

2.5.3 Decision Tree (DT) and Random Forest (RF) Machine Learning Algorithms

The decision trees (DT) algorithm is a classification method that provides the possible outcomes of a series of related choices in a decision map. A DT usually starts with a single node, expands in a few branches, and leads to possible outcomes. Usually, the DT algorithm is used in discussion to map out the best possible decisions mathematically.

The random forest (RF), on the other hand, is an algorithm that works by combining multiple decision trees to increase the accuracy of the generated thematic maps. It is a learning algorithm for classification and solving regression problems (Abdi, 2020). A classification is a form of supervised learning which determines the linkages between the input and output data through repetitive training (Pisner and Schnyer, 2019). Through the

classification, features related to a set of examples are further utilized for training a decision function that generates class assignments with a given accuracy. Furthermore, the RF is one of the most used learning algorithms (Belgiu and Drăgu, 2016) due to its robustness against overfitting and ease of parametrization (Kavzoglu, 2017).

2.5.4 Support Vector Machines (SVM) Learning Algorithm

Similar to RF, the support vector machine learning algorithm is commonly used for classification or regression challenges. A comparison of the performance of the three classifiers is shown in Table 2.5 (Kavzoglu et al., 2020). In this comparison, the algorithms were used in the classification of satellite images to identify forest, grass, asphalt road, soil and bare area, urban and water. The result shows that SVM has the best performance, with the highest overall accuracy of 95.17%, followed by the RF (94%) and the DT (85.44%).

	Dataset - I		Dataset - II		Dataset - III	
	OA (%)	Kappa (%)	OA (%)	Kappa (%)	OA (%)	Kappa (%)
SVM	93.22	91.87	89.44	87.33	95.17	94.20
RF	92.39	90.87	88.56	86.27	94.00	93.80
DT	85.44	82.53	78.56	74.27	83.56	80.27

Table 2.5: Comparison of the three classifiers in terms of overall accuracy and kappa values (Kavzoglu et al., 2020).

SVM has also been reported to be competent at analyzing triboelectric output signals with high performance (Wu et al., 2018), which has been used in

applications such as a virtual keyboard (Luo et al., 2021) and machine fault detection (Li et al., 2020).

2.5.5 Examples of A.I. in TENG

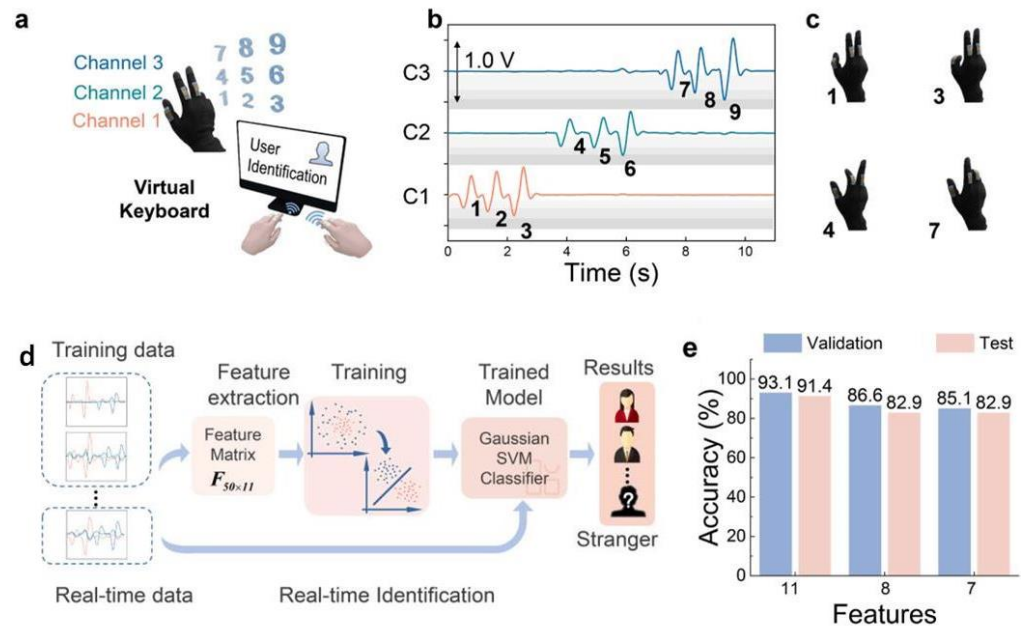


Figure 2.11: (a) Triboelectric based smart glove as a virtual keyboard. (b) Real-time signal output from 9 different finger motions which represent number 1-9. (c) Example of finger motions to represent number 1, 3, 4, and 7. (d) The process flow of the training and real-time identification. (e) Classification accuracy from 11, 8, and 7 features (Luo et al., 2021).

Figure 2.11 (a) represents an example of A.I. in TENG that functions as a glove-based multi-dimensional HMI (Luo et al., 2021). The developed glove-based HMI can real-time translate nine different finger motions representing numbers 1-9 through electrical signals (Figure 2.11 (b)). Examples of finger motions are presented in Figure 2.11 (c). In the experiment, 350 sets of data were obtained from seven different researchers (50 from each researcher) and were sent to an SVM learning algorithm for classification with a validation (training) to testing ratio of 9:1 (Figure 2.11 (d)). After the training, the

classification accuracy of the developed HMI reached 93.1% (Figure 2.11 (e), which shows its potential as a solution for intuitive multi-dimensional HMI.

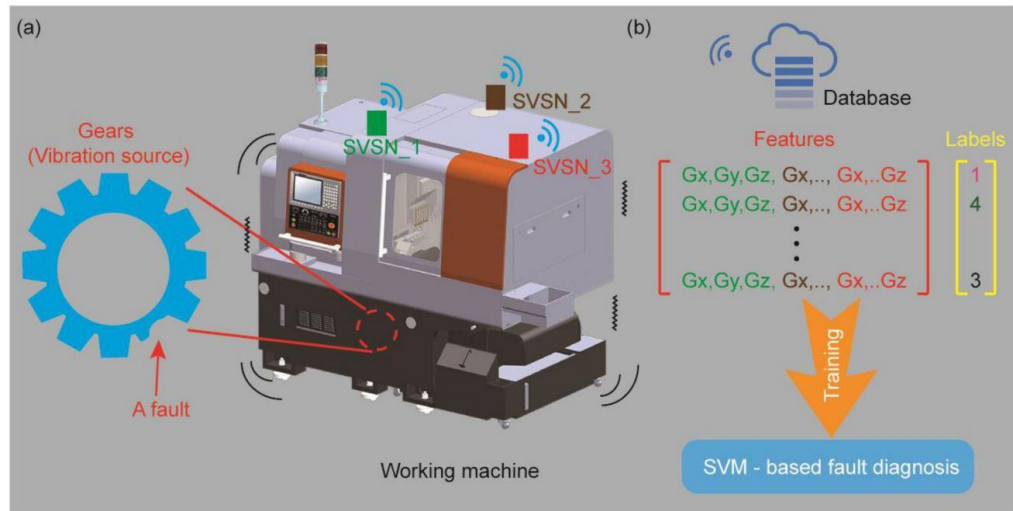


Figure 2.12: SVM algorithm-based machine fault detection using a multi-nodes triboelectric sensor network. (a) Schematic diagram of the machine fault detection system. (b) The structure of the database for SVM-based fault detection (Li et al., 2020).

Another example of A.I. in TENG is shown in Figure 2.12. Li et al. developed an SVM algorithm-based machine fault detection system using a multi-modes triboelectric sensor network (Li et al., 2020). Figure 2.12 (a) shows the schematic diagram of the machine fault detection system, and Figure 2.12 (b) represents the database structure for SVM-based fault detection. The developed multi-modes triboelectric sensor network can identify working machine conditions by analysing the acquired acceleration and temperature data. Each working condition (charging, working, stopping) was repeated 500 times, and the obtained data were sent to an SVM learning algorithm for classification with a training to testing ratio of 3:1. After the training, the developed system provided an accuracy of 83.6% in identifying the different working conditions of the machine.

2.6 Conclusion

In this section, the importance and the comparison of self-powering mechanisms have been reviewed. Compared with the previous literature on PG and TENG, TENG provides a better option for designing the pressure sensor on soft and irregular surfaces. It can be fabricated from materials that are complied with the contact surfaces. On top of that, TENG's four fundamental working methods have been reviewed and compared. Based on the literature review, we designed our first sensor in spiral design microfluidic channel in freestanding mode. This approach offers more space-efficient than the previous device mentioned in the literature (Shi et al., 2016). For our second device, vertical contact separation mode was used to comply with a soft robotic gripper.

Besides, the operating parameters and the constructing materials for a stretchable TENG are comprehensively studied. Our pressure sensors were fabricated from stretchable elastomers, which have a greater conformal contact on human skin and soft robotic than other solid-state TENG-based pressure sensors. Numerous literature works have been reviewed to compare the advantages and disadvantages of using surface and porous enhancement methods. Based on the literature, we introduced porous structures in our second pressure sensor to improve its durability compared to the mentioned surface type. Lastly, assisted with an artificial intelligence algorithm, the TENG sensor can be leveraged into a smart system for a more complex decision prediction application.

CHAPTER 3

DESIGN AND DEVELOPMENT OF A STRETCHABLE SELF-POWERED PRESSURE SENSOR BASED ON THE TRIBOELECTRIC PRINCIPLE

3.1 Overview

This chapter reports developing a stretchable TENG-based self-powered pressure sensor using elastomer polydimethylsiloxane (PDMS). The triboelectrification is induced based on the rubber-liquid interaction. As a proof of principle in demonstrating the pressure sensing, the TENG-based sensor was attached to a human finger to function as a touch button for the HMI application. The touch button was used to control a real-time light-emitting diode illumination and gaming interaction. Unlike the conventional touch button that only produces a binary output, this compact touch button can emulate a real-time impact event from the applied pressure. Utilizing microfluidic techniques with a compact design, the developed sensor is space-efficient and effective in sensing fingertip pressure.

3.2 Design and Working Principle

Figure 3.1 (a) shows the schematic of the proposed soft pressure sensor that is being attached to the fingertip for touch-button application. The soft

pressure sensor is designed similarly to a micropump structure (Chee et al., 2012; Mohd Ghazali et al., 2017; Rusli et al., 2018). It consists of a deionized (DI) water-filled chamber (diameter = 5 mm and height = 3.5 mm) connected to a spiral shape microchannel. The soft pressure sensor is made of polydimethylsiloxane (PDMS) material, a soft and stretchable material. Here, a thin PDMS membrane is bonded on top of the chamber to transfer the externally applied pressure when in contact with the pre-filled DI water contained inside the chamber.

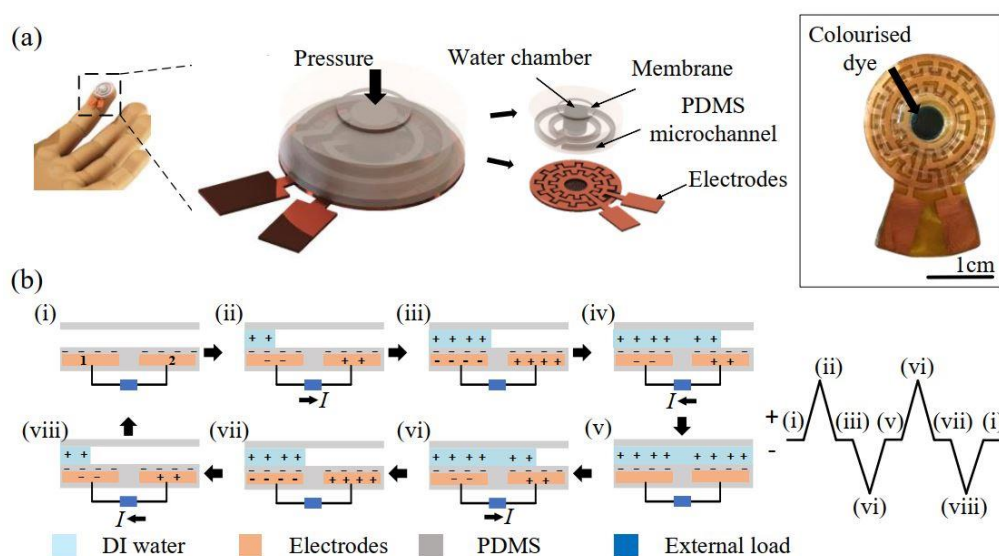


Figure 3.1: (a) Schematic illustration of the triboelectric-based soft pressure sensor. The inset is a photograph of the device. (b) Detailed operation principle of the soft pressure sensor. The periodic flow of water back-and-forth (i–ii–iii–iv–v–i) in the microchannel produces a triboelectric signal between the two electrodes.

A pair of spiral-shaped interdigitated electrodes fabricated using the copper-clad polyimide (thickness = 30 μm) are coated with a thin PDMS layer and bonded with the microchannel to form an enclosed platform. The triboelectric output can be measured from the electrode pair. Unlike the straight

microchannel design (Shi et al., 2016), this design allows a smaller footprint and can be bonded conformably on a fingertip.

The pressure sensor works based on contact electrification during the PDMS–water interaction to produce triboelectric output. The DI water and the elastomer PDMS are used as the positive and negative materials in this design. Figure 3.1(b) shows the working principle of the microfluidic-based pressure sensor. Figure 3.1(b)-(i) shows that when no pressure is exerted on the pressure sensor, the pressure sensor is at its neutral state. The positive charges balance the negative charges from the PDMS surface in the DI water. The membrane deflects downward when external pressure is applied to the soft pressure sensor. It creates compression pressure to displace the DI water flow from the chamber into the microchannel (Figure 3.1(b)-(ii)). The negative ions in the DI water are absorbed onto the PDMS surface and form negative triboelectric charges on the PDMS surface. This induces a potential difference between the electrodes and causes an electrical current to flow from the first electrode to the second electrode. A positive output peak is then produced. When the DI water continues to flow and contacts with the second electrode, a higher potential is induced in the second electrode, and it causes the current to flow in the reverse direction (Figure 3.1(b)-(iii)) until a new equilibrium is reached. When the external pressure is released, the DI water in the microchannel siphons back to the chamber. The triboelectric mechanism is repeated but in the reverse direction (Figure 3.1(b)-(iv) and (v)).

3.3 Numerical Simulation and Fabrication of Sensor

To have a more quantitative illustration of the liquid–rubber electrification, a finite element modelling was performed using COMSOL Multiphysics (Figure 3.2(a)). The soft pressure sensor is modeled with DI water flows in a 1 mm thick microchannel. Electrostatic physics was selected for the simulation with a normal-sized mesh setting. Water is more electropositive than PDMS based on triboelectric series (Zou et al., 2019). Therefore, the DI water layer is assigned as the positive layer with a charge density of 0.008 pC m^{-2} at the contacted boundary layer. The charge density of the material is measured using an electrometer (Keithley 6514, USA) under room temperature and relative humidity of 40%. PDMS layer is set at zero charges as a reference layer in the simulation.

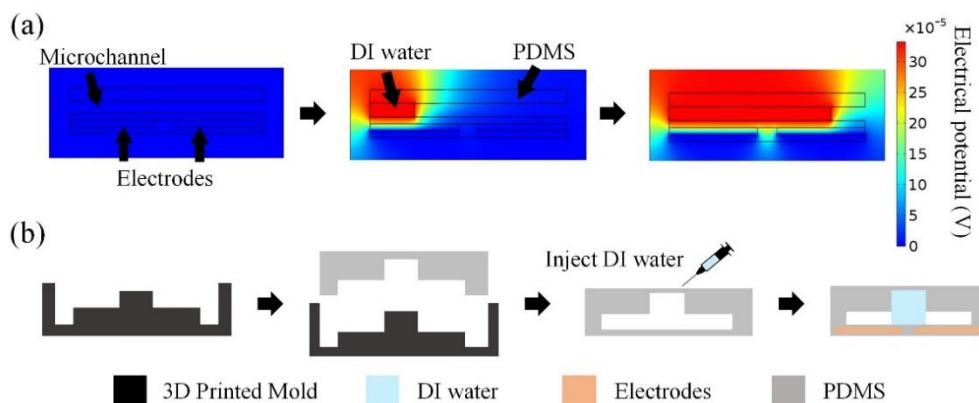


Figure 3.2: (a) Simulation of electrical potential distribution in the water and PDMS triboelectric layers using COMSOL Multiphysics. (b) The fabrication process of the soft pressure sensor.

Figure 3.2(a) shows no potential difference in the absence of DI water initially. When DI water flows in the microchannel, a potential difference is induced due to the charge transfer mechanism. The gradient in the charge

density produces a flow of electrical current according to the fluidic motion in the microfluidic channel. The simulation showed that the microfluidic-based TENG could replace the spatial separation distance in a conventional TENG pressure sensor with a charge transfer mechanism between the liquid-solid interfaces. Figure 3.2(b) shows the fabrication process of the soft pressure sensor. First, a spiral shape microchannel mold was fabricated using a 3D printer. A PDMS solution, mixed with a ratio of 1 (hardener):10 (resin), was poured into the 3D printed mold. Then, the PDMS solution was degassed in a vacuum chamber and was left to cure at 75 ° C in an oven for 60 minutes. The fabricated PDMS microchannel was removed from the 3D printed mold, and an enclosed microchannel was formed by bonding it with another 0.1 mm thick PDMS layer using some ARclad® IS-8026 silicone transfer adhesive. Lastly, a pair of interdigitated electrodes were formed by etching a copper-clad polyimide flexible printed circuit board (PCB) (AP9121, Pyralux Polyimide Film, DuPont, Singapore). The soft pressure sensor was constructed by bonding the microchannel and the interdigitated electrodes. Lastly, the interdigital patterned flexible PCB was pasted below the PDMS microchannel as electrodes.

3.4 Results and Discussion

3.4.1 Experiment Setup

As mentioned in section 2.3.3, the movement amplitude and frequency of the applied pressure are two crucial parameters to influence the generated output. Higher compression frequency will result in a higher flowing speed of

the DI water flowing across the interdigitated electrodes. A mechanical shaker (TIRA GmbH S 521, Germany) coupled with a customized metal rod was used to generate continuous pressure to the soft pressure sensor (shown in Figure 3.3(a)). Figure 3.3(b) illustrates that the mechanical shaker was positioned at some distance from the pressure sensor to minimize the noise that the shaker could generate. The parametric settings of the mechanical shaker, as shown in Figure 3.3(c), were configured through software (Vibration Research Medallion II Vibration Control, USA) and an amplifier (TIRA GmbH BAA 120, Ashly Audio, USA). The triboelectric principle features high voltage and ultra-low current behavior (Wang et al., 2019). It might be challenging to measure the ultra-low current changes using a commercial portable data acquisition module. To fit for HMI purposes, the output voltage from the soft-pressure sensor was acquired using a NI Elvis board (NI-ELVIS Series II, USA) to better correlate with the input pressure.

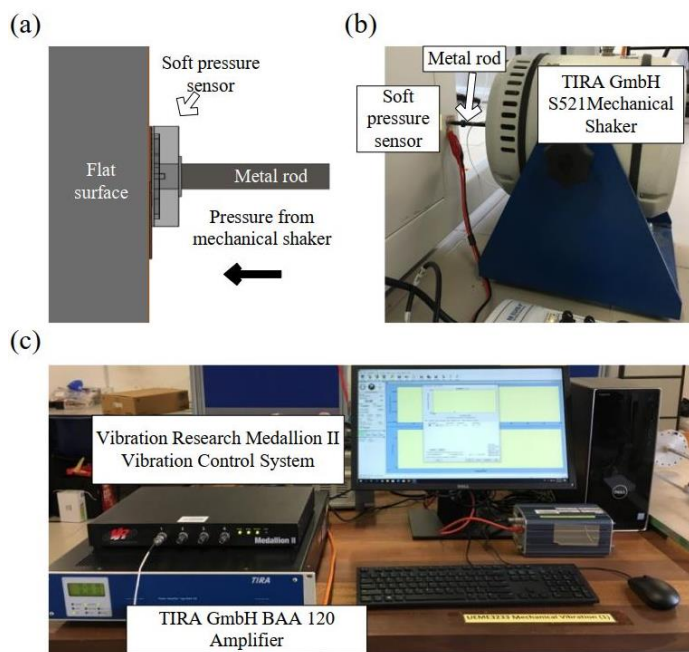


Figure 3.3: (a) Solidwork drawing of the experiment setup. (b) The experimental setup with the mechanical shaker. (c) The vibration configuration system.

3.4.2 Characterisation of Self-Powered Pressure Sensor

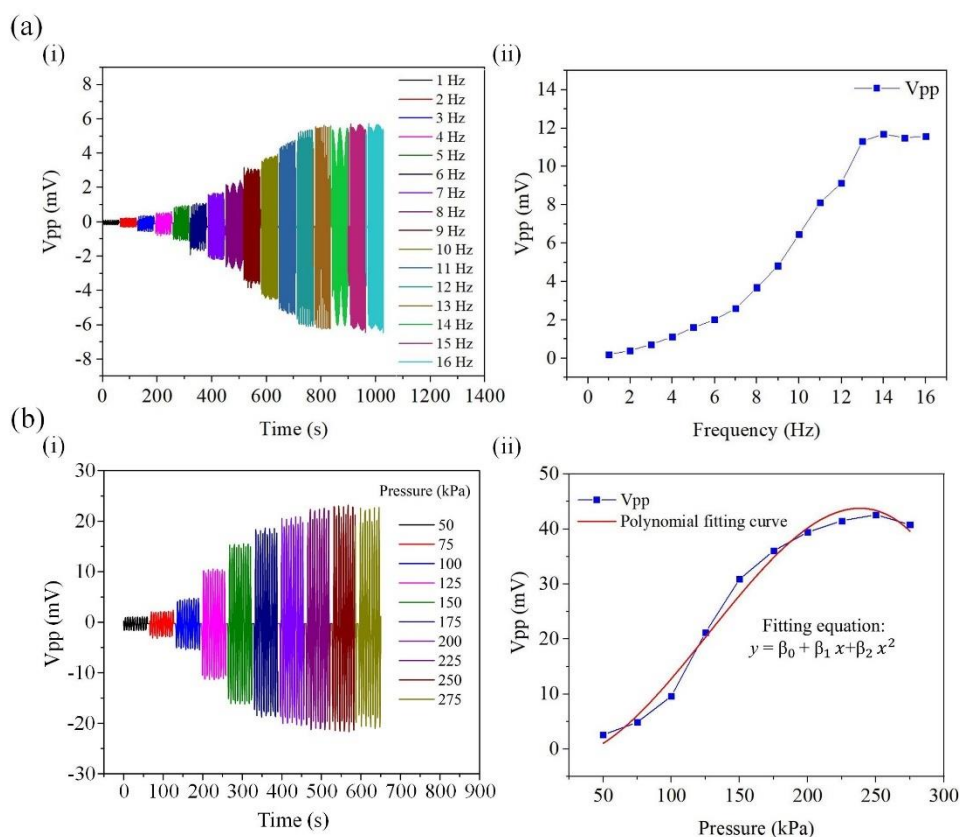


Figure 3.4: (a)-(i) Temporal response of the triboelectric output from 1 Hz to 16 Hz under a constant input pressure of 50 kPa. (ii) Trendline of output voltage, V_{pp} at a different frequency. (b)-(i) Temporal response of the voltage output at different input pressure ranging from 50 kPa to 275 kPa under a fixed frequency at 7 Hz. (ii) Trendline of the output voltage, V_{pp} at different input pressure.

The frequency dependency of the pressure sensor was first tested by setting the mechanical shaker's frequency ranges from 1 to 16 Hz with an increment of 1 Hz. The input pressure to the pressure sensor was kept at a constant pressure of 50 kPa. As shown in Figure 3.4(a)-(i), repetitive triboelectric output at each operating frequency shows that the pressure sensor's output performance is reliable. In addition, the positive peak and negative peak for each cycle are almost symmetrical, indicating that the forward flow rate and the backward flow rate of DI water in the microchannel are the same. This

phenomenon has also verified no water leakage under continuously applied pressure. Figure 3.4(a)-(ii) summarizes the pressure sensor's frequency dependency behavior. The maximum triboelectric output voltage is up to V_{pp} , 11.5 mV.

The output voltage saturates when the input frequency increases beyond 13 Hz. The DI water cannot flow back to the chamber due to the membrane's fast compressing movement. In this case, the DI water may only vibrate at a fixed position. The magnitude of the triboelectric output can determine the pressure applied to the soft pressure sensor. The same experimental setup was performed, except the frequency was fixed at 7 Hz with the input pressure ranging from 50 kPa to 275 kPa. Figure 3.4(b)-(i) shows that the output voltage of the pressure sensor increases with the applied pressure. Higher input pressure creates a higher stroke volume to displace a higher volume of DI water flowing through the electrodes. A polynomial fitting curve and its fitting equation:

$$y = \beta_0 + \beta_1 x + \beta_2 x^2 \quad (3.1)$$

is generated in Figure 3.4(b)-(ii) to obtain the numerical relationship between the V_{pp} and input pressure. From equation 3.1, the parameter β_0 is the y-intercept, β_1 and β_2 are the slope coefficients to determine the error percentage, and x is the corresponding input pressure. However, it shows a declination on the fitting curve when the input pressure increases more than 225 kPa, while there is no significant change (less than 5%) in the output voltage when the pressure further increases. This behavior occurs because the maximum

compression stroke at the chamber is achieved. Higher triboelectric output is anticipated with a larger chamber design.

Besides, the soft pressure sensor has been proven to be very robust. As shown in Figure 3.5(a), we performed a mechanical robustness test by setting the shaker to press on the soft pressure sensor continuously for 2920 cycles under input pressure of 50 kPa with the operating frequency of 0.5 Hz. It was found that the soft pressure sensor could generate a stable output voltage signal of $V_{pp} = 0.37$ mV after 2920 cycles.

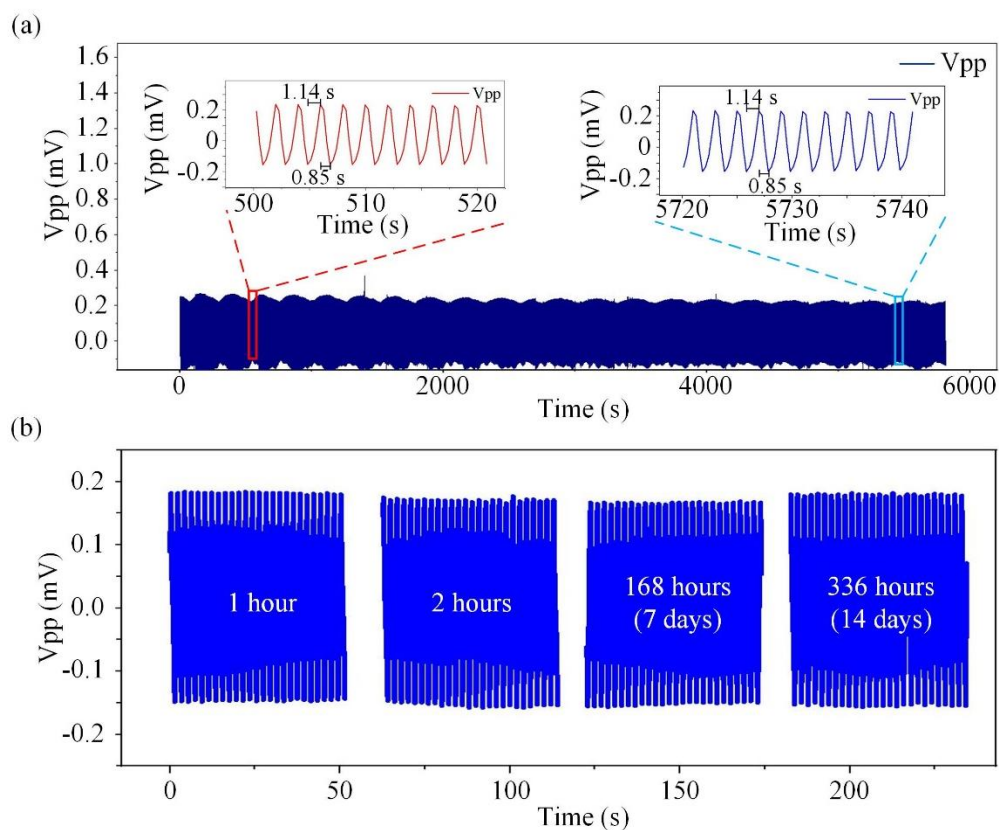


Figure 3.5: (a) Mechanical durability test under 2920 repeated cycles with input pressure of 50 kPa. (b) Stability test of the sensor after 1 hour, 2 hours, 168 hours (7 days) and 336 hours (14 days).

The output voltage, V_{pp} of 500th–520th and 5720th–5740th seconds of mechanical pressing, are shown in the inset of Figure 3.5(a). The response and

recovery time of the sensor were measured to be 1.14 s and 0.85 s, respectively. The response and recovery time were observed to have no noticeable devaluation after a continuous pressing of 2920 mechanical cycles, further validating that the soft pressure sensor can deliver a very stable voltage output for a long operation. To further explore the stability of the sensor, the output voltage of the sensor was measured for 1 hour, 2 hours, 168 hours (7 days) and 336 hours (14 days) under operating frequency and compression force of 0.5 Hz and 50 kPa, respectively. The response of the sensor is presented in Figure 3.5(b). It shows no significant change in the output voltage, ensuring good stability and reliability.

3.4.3 Application of Human-Machine Interface (HMI)

The fabricated soft pressure sensor was attached to the fingertip to control the light-emitting diode (LED) brightness and gaming interface as proof of the HMI function. Figure 3.6(a) shows the functional components used to control the HMI. First, the applied pressure was converted into a triboelectric output signal when a touch event was detected. Next, the output signal was fed into an analog input module of a microcontroller unit for data processing and noise filtering through computer codes written in the Arduino IDE environment. The analog output module then captured the processed data and fed it to an LED. Finally, the intensity of the LED was quantified through ImageJ (a Java-based image processing program).

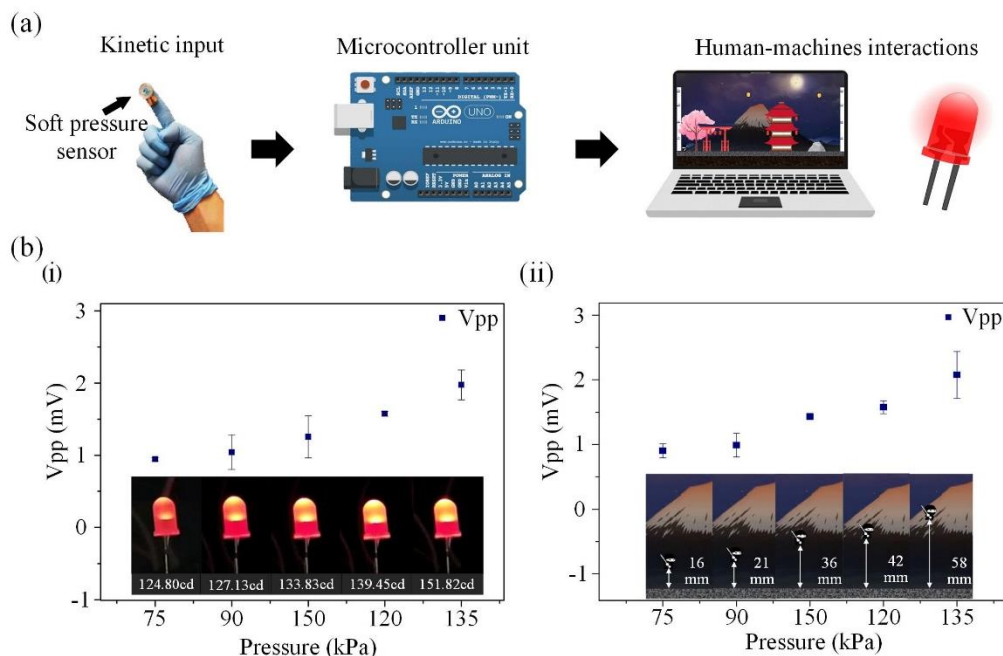


Figure 3.6: (a) The functional component of the HMI. (b)-(i) Output voltage against input pressure in controlling the LED light intensity (shown in the inset). (ii) Output voltage against input pressure controls the jumping height of a ninja character (shown in the inset).

The experiment was conducted under 0.5 Hz of tapping pressure for 20 cycles. Figure 3.6(b)-(i) shows that the LED's intensity increases when the tapping force rises. For example, the LED intensity increased from 124.80 cd to 151.82 cd when the input pressure increased from 75 kPa to 135 kPa. The real-time output voltage from the pressure sensor is also included in the plot to understand the touch stimuli better. The output voltage follows the same trend as the light intensity. The second demonstration used the soft pressure sensor to control a ninja character's jumping height through a designed game. The game was programmed using Unity Engine (Unity Technologies, USA) and displayed through a laptop interface. The jumping height of the ninja character in the game was recorded and measured using ImageJ. As shown in Figure 3.6(b)-(ii), by tapping the pressure sensor with a larger pressure, the ninja jumps from 16 mm

to 58 mm. The jumping height and the output voltage increase with the taping force.

3.5 Summary

A self-powered, wearable, and stretchable microfluidic-based triboelectric pressure sensor has been developed. The microfluidic platform enables triboelectrification during the PDMS–water interaction without considerable hysteresis. The fabricated pressure sensor can detect an input pressure of 50 kPa. The fabricated soft pressure sensor has been proved to be able to operate for a long loading condition, where no noticeable sign of signal deterioration is noticed after 2920 loading cycles. Owing to the compact dimension and soft surface, the sensor can be attached to the fingertip for human-machine interaction. This design is more space-efficient than the reported sensor in the literature (Shi et al., 2016). It shows remarkable performance in controlling the bulb's brightness and a ninja jump in a gaming interaction with a data acquisition unit. The developed pressure sensor aligned with our objective of exploring self-powering mechanisms based on the contact electrification principle for pressure sensing on human skin.

CHAPTER 4

A PARAMETRIC STUDY OF A SPONGE-BASED TRIBOELECTRIC PRESSURE SENSOR

4.1 Overview

The previous chapter presented a wearable, self-powered, stretchable triboelectric pressure sensor capable of detecting finger input pressure. However, the challenge faced is the saturation of generated output when the maximum compression stroke at the water chamber has been achieved, limiting the sensor from sensing a larger pressure input source such as hand tapping motion. Therefore, to improve the sensitivity of a soft pressure sensor in human pressure sensing, a physical modification was introduced in our 2nd pressure sensor prototype. A stretchable sponge-based triboelectric energy harvester (SBTENG) is proposed in this chapter to detect pressure and harvest energy from hand tapping motion. Numerical simulation is performed to study the impact of the sponge-based structure in enhancing the charges in the TENG. The developed stretchable TENG is made of a composite material that consists of eutectic gallium- indium (EGaIn) and Ecoflex. Sodium chloride (NaCl) was used to create porosity in the triboelectric layer. The SBTENG can generate a momentary power of ~5 mW (momentary power density = 99.47 $\mu\text{W}/\text{cm}^2$). The achieved momentary power density is greater than reported porous

polydimethylsiloxane/lead zirconate titanate-based energy harvesters (Ma et al., 2018). An experiment was performed to investigate the relationship between NaCl concentration and the output power. A proof-of-concept experiment shows that the developed stretchable TENG can power up LEDs by harvesting energy from hand tapping motion. This study provides a good design guideline for the sponge-based triboelectric layer.

4.2 Design of SBTENG

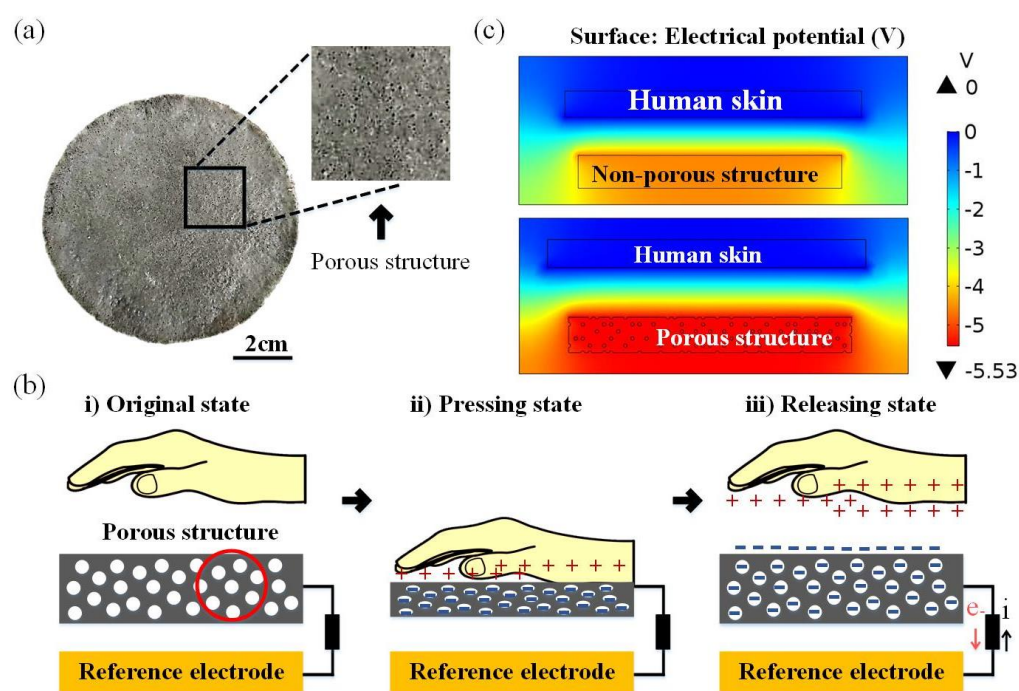


Figure 4.1: (a) Top view of the fabricated prototype. (b) Schematic illustration of the working mechanism of the SBTENG, (i) Original state, (ii) Pressing state, and (iii) Releasing state. (c) COMSOL simulation result of the non-porous structure and porous structure.

Figure 4.1(a) shows a fabricated sponge-based triboelectric energy harvester (SBTENG). The prototype was designed in a cylinder shape, with a surface contacting area with a dimension of 50.3 cm^2 (diameter = 8 cm) and a

thickness of 1 cm. The SBTENG consists of two triboelectric layers, human skin (positive triboelectric layer) and an EGaIn-Ecoflex composite layer (negative triboelectric layer). The EGaIn-Ecoflex composite layer also acts as a compliance electrode for charge transfer. Compared with the effort that uses carbon black (Xiao et al., 2018) as the compliant electrode, EGaIn (68.5% Ga, 21.5% In, 10% Sn by weight) can avoid agglomeration issues due to its liquid form physical state. Mixing the EGaIn in the Ecoflex- 0050 elastomer makes the elastomer a conductive medium. At the same time, it maintains the elastic properties of the elastomer. This elastic feature is essential to ensure the conformity of the wearable energy harvester.

4.2.1 Working Principle of SBTENG

Figure 4.1(b) shows the working principle of the SBTENG. SBTENG operates based on the single electrode triboelectric mode principle (refer to Figure 4.1(b)(i)). This working mode requires an external reference electrode for charge transfer. In our case, we use a 50 cm × 50 cm copper plate as the reference electrode. When human skin presses on the surface of the SBTENG in the normal direction (shown in Figure 4.1(b)(ii)), the electrons are transferred from the human skin to the EGaIn-Ecoflex composite layer, forming a positively charged layer at the human skin surface. This charge transfer phenomenon is due to the difference in charge affinity when the two materials are in contact. Figure 4.1(b)(iii) shows that a complete close-loop can be formed when an external load is connected with the negatively charged EGaIn-Ecoflex composite layer and the external copper plate.

4.2.2 Numerical Simulation

Figure 4.1(c) shows the numerical simulations for the porous (SBTENG) and non-porous energy harvesters using COMSOL Multiphysics. Electrostatic physics was selected in the simulation with a normal-sized mesh setting. Based on the triboelectric series (Zou et al., 2019), silicon rubber is more electronegative than human skin. Therefore, the EGaIn-Ecoflex composite layer is assigned as the negative layer with a surface charge density of -34.18 pC m^{-2} at the top boundary layers of the non-porous and porous structures. The surface charged density is measured using an electrometer (Keithley 6514, USA) under room temperature and relative humidity of 40%. The human skin layer is set at zero charges as a reference layer in the simulation. Simulations show the porous structure has a more significant potential difference (wider and darker red colour zone) than the non-porous structure (narrower and lighter red colour zone). This has verified that the porous formed in the structure can trap more charges than the non-porous structure due to its advantage of a large surface area to volume ratio.

4.3 Fabrication of Sensor

Figure 4.2 shows the fabrication processes for SBTENG. First, a cylindrical mold was printed using the acrylonitrile butadiene styrene (ABS) material. Then, 22% (6.5 g) of Ecoflex 00-50 solution was mixed with 13% (4 g) of EGaIn. Another 19.5 g of NaCl particles (Merck & Co., USA) were then

added to the mixture solution, which had occupied 65% of the total mixture (Figure 4.2(a)).

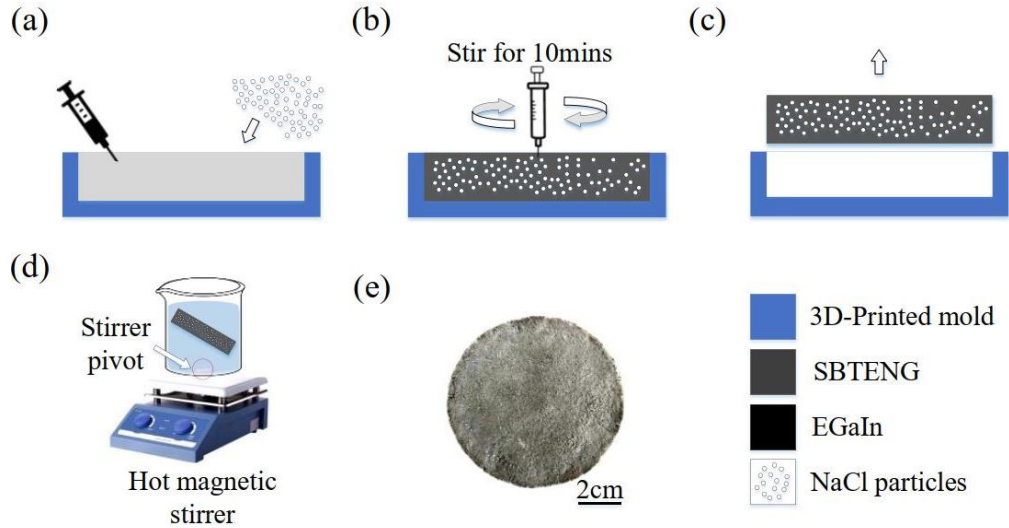


Figure 4.2: The fabrication processes of the SBTENG. (a) Solutions were added into a 3D-printed mold. (b) A syringe was used to stir and mix the components. (c) The cured prototype was carefully removed from the mold. (d) The prototype was immersed in deionized water to dissolve the NaCl particles. (e) The end product of the fabrication processes.

The NaCl particles would act as a sacrificial medium for porous formation. The porosity of the structure is highly relying on the volume of the NaCl particles, according to the porosity equation,

$$\emptyset = \frac{V_V}{V_T} \quad (4.1)$$

where, V_V is denoted as void volume (volume of NaCl particles), and V_T is the total volume of the mixture. Next, the mixture was stirred thoroughly for 10 minutes until it showed a homogenous colour (Fig. 2(b)). The mixture was left

to cure for 6 hours at 70 °C. Later, the prototype was removed from the 3D printed mold carefully, assisted by the isopropanol solution (shown in Fig. 2(c)). The cured prototype was immersed in deionized water at 60 °C for 8 hours to dissolve the NaCl particles (Figure 4.2(d)). Finally, as shown in Figure 4.2(e), the porous was formed in the SBTENG. The fabrication steps were repeated with 0% (as the control), 25%, 45%, and 65% of NaCl concentrations, to study the dependency of the output power on the pores concentration. Figure 4.3 shows the scanning electron microscope (SEM) images of the conductive Ecoflex with four different concentrations, starting from 0% (Figure 4.3 (a)), 25% (Figure 4.3 (b)), 45% (Figure 4.3 (c)) and 65% (Figure 4.3 (d)). Based on the images, the average size of the created porous structures is ~ 350 μm .

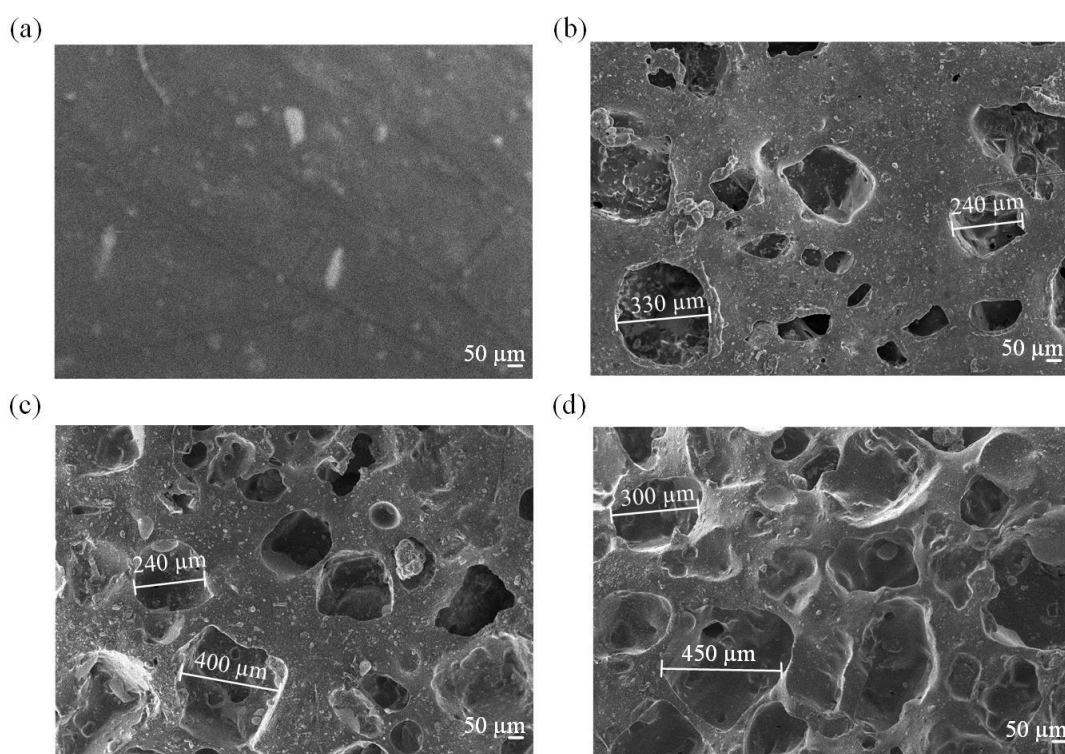


Figure 4.3 SEM images of cross-section of the conductive Ecoflex with (a) 0% concentration of NaCl particles, (b) 25% concentration of NaCl particles, (c) 45% concentration of NaCl particles, and (d) 65% concentration of NaCl particles.

4.4 Experimental Result and Discussion

4.4.1 Experiment Setup and Sensor Characterisation

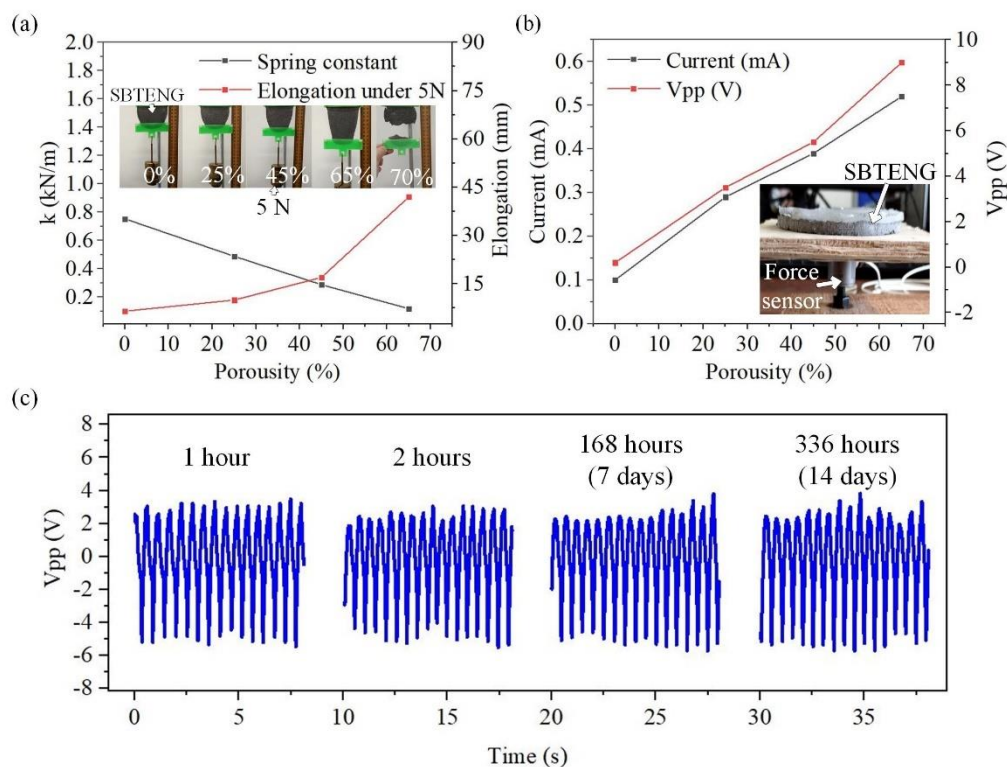


Figure 4.4: (a) Study of the spring constant and elongation (under 5 N) with different NaCl concentration, ranging from 0% (non-porous), 25%, 45%, 65% to 70%. The inset of the figure represents the experimental setup for measurement. (b) Study of the output voltage and current with different NaCl concentration (0%, 25%, 45% and 65%) under a constant 25 N compression force. The inset of the figure represents the experimental setup for measurement. (c) Stability test of the sensor (65% NaCl concentration) after 1 hour, 2 hours, 168 hours (7 days) and 336 hours (14 days).

The spring constant of the soft sensor is crucial in determining the deformation behaviour of the sensor when an external force is applied. Thus, an experiment has been conducted to determine the spring constant of SBTENG with different porosity percentages (NaCl concentration), ranging from 0%, 25%, 45%, 65%, to 70%. The experiment setup consists of 3D printed clips that connect the sensors with a 5 N slotted weight in a vertical orientation, as shown

in the inset of Figure 4.4(a). Figure 4.4(a) shows that the spring constant of the sensors decreased from 0.75 kN/m to 0.17 kN/m when the porosity increased from 0% to 65%. However, when the porosity increased to 70%, the sensor eventually lost its spring constant and fractured during the experiment. Another experiment was conducted to determine the electrical output performance of the sensor with different porosity. The measurement was recorded using NI Elvis II+ (National Instrument, United States) and processed in NI LabView software. As shown in the inset of Figure 4.4 (b), the SBTENG was placed on the force sensor (Dytran series 1051, USA). The output of the force sensor was fed to CAN-MD® Console software, and the hand-tapping force was maintained at 25 N~30 N throughout. As mentioned in the previous experiment, the sensor with 70% porosity eventually lost its spring constant and fractured during the experiment. Therefore, the electrical output measurement was only conducted up to 65% porosity. Figure 4.4 (b) shows that the output voltage, V_{pp} and current output increase with the porosity percentage. A low output V_{pp} (approximately 0.1 V ~ 0.2 V) can be observed for the non-porous (0% NaCl concentration) sample in Figure 4.4 (b). The output voltage was improved to 9 V with 65% porosity, with an increase factor of 40 times. The output current improved to 0.6 mA with the 65% porosity, which is an increase factor of 3 times compared with the current output of the non-porous sample (0% porosity). This concludes that the increase of the porosity improves the electrical output. To further explore the stability of the sensor, the output voltage of the sensor with 65% porosity was measured for 1 hour, 2 hours, 168 hours (7 days) and 336 hours (14 days) under a consistent hand-tapping force input of 25~30 N. The response

of the sensor is presented in Figure 4.4(c). It shows no significant change in the output voltage, ensuring good stability and reliability.

4.4.2 Demonstration on Energy Harvesting Using SBTENG

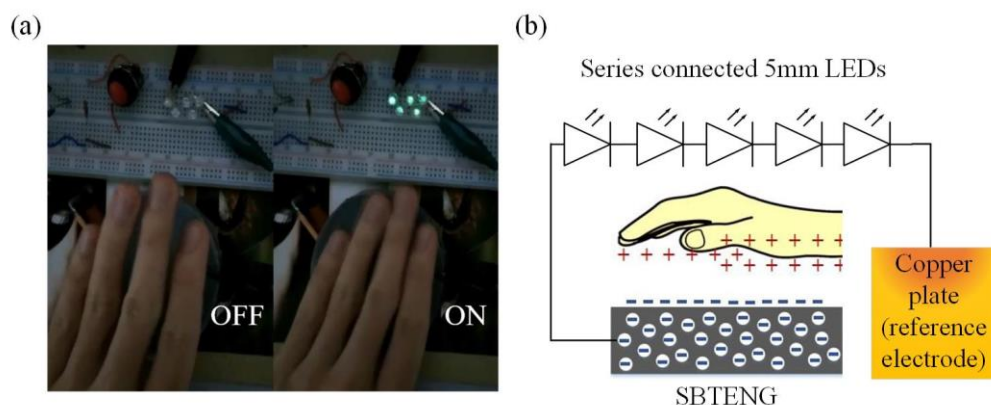


Figure 4.5: (a) Demonstration of SBTENG to power up 5 LEDs by harvesting hand-tapping kinetic energy. (b) Schematic illustration of the circuit connection.

Figure 4.5 (a) shows that our developed SBTENG can light up five series-connected LEDs (5mm green LED). The circuit connection for the demonstration is presented in Figure 4.5 (b), consisting of 5 LEDs, SBTENG and a 50 cm \times 50 cm copper plate as the reference electrode. This proof-of-concept study shows the great potential of our developed SBTENG in powering up small, wearable electronic gadgets.

4.5 Summary

A soft, stretchable, and human skin-activated sponge-based triboelectric energy harvester (SBTENG) was fabricated. Different from the microfluidic freestanding mode pressure sensor in Chapter 3, which has a compact design

and is applied for measuring fingertip pressure and HMI application, SBTENG was applied to perform hand tapping pressure sensing and energy harvesting. Its dependency on the porosity was characterized and has been numerically proven that the potential difference of the porous-based structure is higher than the non-porous-based structure. This is due to the trapping of electrical charges in the porous structure and the larger contact surfaces. To validate the simulation results, experimental measurements have been performed to study the electrical outputs under different NaCl concentrations (0%, 25%, 45%, and 65% of total volume). These concentrations correspond to different porosity values. An experiment has shown that the electrical output increases with the porosity value, validating our hypothesis. More charges can be trapped in our energy harvester with a higher porosity level, which contributes to a larger potential difference. The experiment results obtained from the 65% porosity level sample have increased by 40 times compared to the non-porous (0% NaCl concentration) sample. The SBTENG can generate a momentary power of ~ 5 mW (momentary power density = $99.47 \mu\text{W}/\text{cm}^2$). The momentary power density is more significant than reported porous polydimethylsiloxane/lead zirconate titanate-based energy harvesters (Ma et al., 2018). Lastly, the developed stretchable TENG can power up LEDs by harvesting energy from hand tapping motion.

CHAPTER 5

STRETCHABLE, SELF-POWERED PRESSURE SENSOR FOR PNEUMATIC SOFT GRIPPER PICK-AND-PLACE SYSTEM

5.1 Overview

As demonstrated in chapter 4, the sponge-based stretchable pressure sensor has successfully proven its improved output performance in sensing human hand tapping motion. This chapter leverages the sponge-based stretchable pressure sensor (with 65% of NaCl concentration) to a soft robotic system by attaching it to a pneumatic actuated smart soft robotic gripper. The signals collected from the gripped objects were then sent to a support vector machine (SVM) learning approach. As a result, the smart gripper can recognize objects with a training accuracy of 91.6%.

5.2 Design of Sensors and Soft Gripper Pick-and-Place System

Figure 5.1 shows the architecture of the triboelectric-based smart gripper. Figure 5.1 (a) represents the contact-separation mechanism of the bending sensor. The sponge-based EGaIn triboelectric layer with 65% NaCl concentration is attached at the joint of the soft gripper, shown in Figure 5.1 (b), to detect the bending angle when the gripper is pneumatically activated. Figure 5.1 (a) depicts the bend and unbend states of the finger. The bend sensors

operate based on the contact separation mode that utilizes the separation gap caused by the expansion of the chamber patterns when the air is injected.

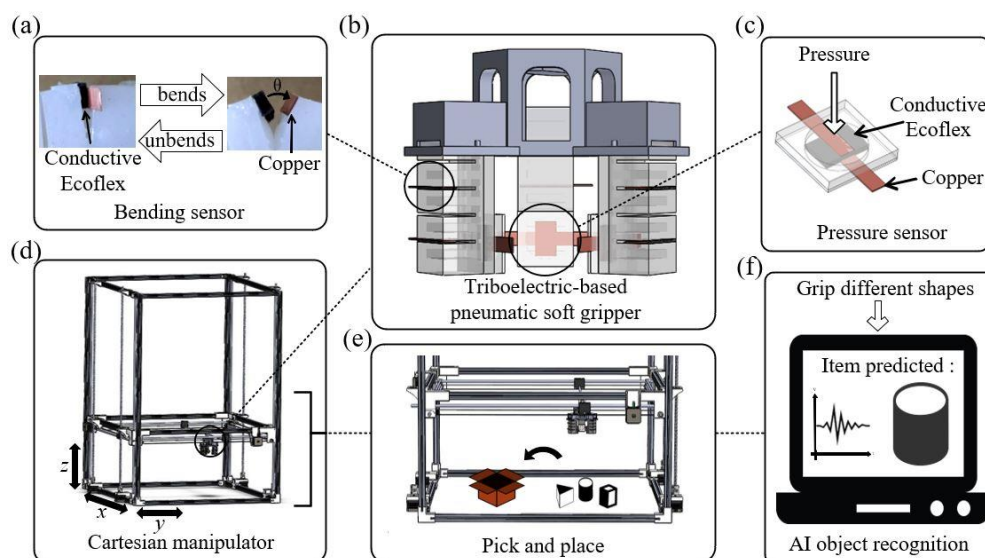


Figure 5.1: (a) Reaction of the fabricated bending sensor when the soft finger bends and unbends. (b) Schematic illustration of the triboelectric-based pneumatic soft gripper. (c) Fabricated pressure sensor based on triboelectric mechanism. (d) Cartesian manipulator with the triboelectric-based pneumatic soft gripper attached. (e) Pick and place application. (f) AI object recognition application.

The fingers of the soft gripper are controlled by the same valve connected to a customized motor-driven pneumatic actuation system. The fingers experience the same pressure input and bending angle with this setup. The bend (area = 1.5 cm x 0.5 cm) and pressure sensors (shown in Figure 5.1 (c), area = 2 cm x 2 cm) consist of two triboelectric layers: a composite layer of EGaIn-Ecoflex (00-50, Smooth-On, Easton, Pennsylvania) as the negative layer, and copper-clad polyimide (thickness = 30 μm) as the positive layer. Both the negative and positive layers were connected to a copper electrode. Like the sensor presented in Chapter 4, the EGaIn-Ecoflex composite layer was designed in a sponge-alike structure (created by sodium chloride (NaCl) sacrificing

method) to improve the output voltage. The mixing of EGaIn in the Ecoflex layer provides electrical conductivity to the sponge-based Ecoflex layer and transfers triboelectric charges. The soft robotic system is attached to a customized three axes cartesian manipulator (Figure 5.1 (d)). As proof of concept, three basic symmetric shapes of objects, including cylinder, cuboid, and pyramid prism, were used as the pick and place product (Figure 5.1 (e)). The measured signal was then fed to a support vector machine (SVM) for object recognition application (Figure 5.1 (f)).

5.3 Device Fabrication

Copper-clad polyimide and sponge-based conductive Ecoflex are chosen as the positive and negative triboelectric materials for both pressure and bending sensor due to the large electron affinity differences (Zou et al., 2019) in these materials. The fabrication of the sponge-based conductive Ecoflex has been discussed in Section 4.3. The simplified fabrication process of the sensors is shown in Figure 5.2.

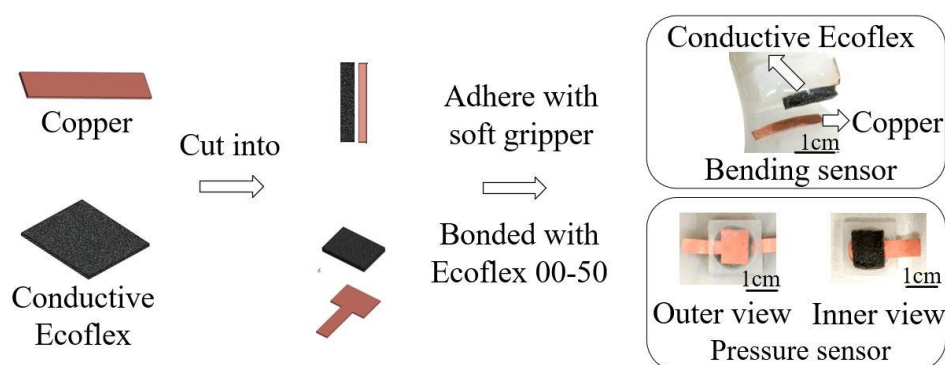


Figure 5.2: The simplified fabrication process of the bend and pressure sensors.

Each of the fingers was attached with two bend sensors on its surface's chamber patterns. The bend sensors were made of copper-clad polyimide (1.5 cm x 0.5 cm) and conductive Ecoflex (1.5 cm x 0.5 cm). It is slotted between the two chambers intervals to detect the angle change on the tip and middle part of the finger when it bends. For the pressure sensors, the conductive Ecoflex and the copper-clad polyimide were cut into 1.5 cm x 1 cm, encapsulated in an Ecoflex mold, and attached to the tip of the soft fingers.

5.4 Working Principle of Sensors

Figure 5.3 illustrates the working principle of the sensors in three different states, (i) the initial state, which indicates the original position of the fingers, (ii) the bending state (gripping state), which represents the state where the gripper bends and contacts with an object, (iii) unbend state (release state), which happens after the gripper release the object.

Both the bending and pressure sensors remain neutral at state (i), as the separation distance between the two triboelectric layers in each sensor is not changing. The fingers bend when the air pumps into the fingers by a motor-driven pneumatic actuation system (state (ii)). In this state, the separation distance of the two layers in the bending angle sensors enlarged. Due to triboelectrification, the negatively charged is induced at the conductive Ecoflex. The copper, on the other hand, is positively charged, causing a potential difference between the two electrodes. Thus, a current will flow from the copper electrode to the ecoflex electrode.

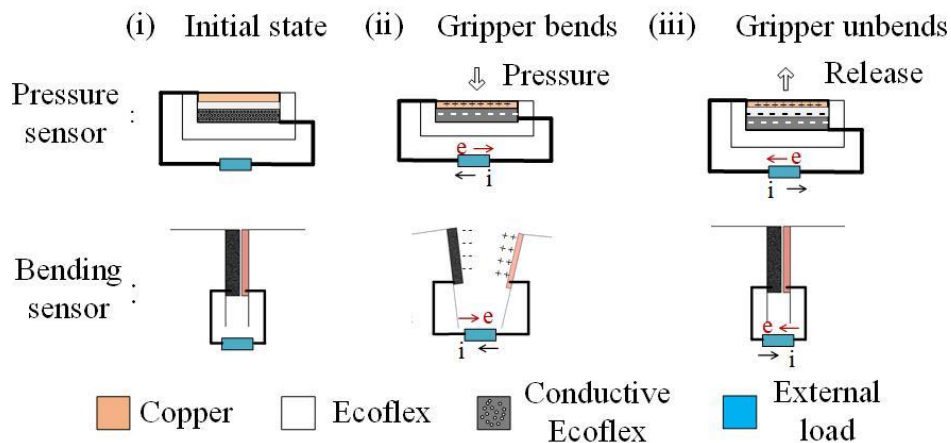


Figure 5.3: Detailed operation principle of the sensors from the (i) initial state to (ii) gripping an object state (Pressure sensor: the two triboelectric layers contact each other as the sensor receives pressure input from the gripped object, bending sensor: two triboelectric layers separate due to the bending motion of soft finger) and finally to (iii) releasing an object state (Pressure sensor: the two triboelectric layers separate as in the result of the removal of the input pressure, bending sensor: two triboelectric layers contact due to the unbending of a soft finger)

For the pressure sensors, the separation distance between the triboelectric layers will be reduced by the input pressure from the targeted object's surface. Hence, a potential difference between the two triboelectric layers occurred and generated a current flow from the ecoflex electrode to the copper electrode. At the released stage (state iii), the injected air is vacuumed and causes the fingers and sensors to revert to their initial state (for pressure sensor: the two triboelectric layers separate as a result of the removal of the input pressure; for bending sensor: two triboelectric layers contact due to the unbending of the soft finger). Therefore, a current is induced and flows in the opposite direction as in the state (ii).

5.5 Numerical Simulation

To have a more quantitative illustration of the potential differences between the triboelectric layers, a finite element simulation was performed using COMSOL Multiphysics (Figure 5.4). Electrostatic physics was selected for the simulation under a normal-sized mesh setting. Based on the triboelectric series (Zou et al., 2019), copper is more electropositive than ecoflex. Therefore, the copper layer is assigned as the positive layer with a charge density of 0.3 pC m^{-2} , measured using an electrometer (Keithley 6514, USA) under room temperature and relative humidity of 40%. Ecoflex layer is set at zero charges as a reference during the simulated triboelectrification. Figure 5.4 (a) represent the potential differences between the two triboelectric layers when the bending angle change from 0° (state “A” in Figure 5.4 (a)) to 60° (state “B” in Figure 5.4 (a)).

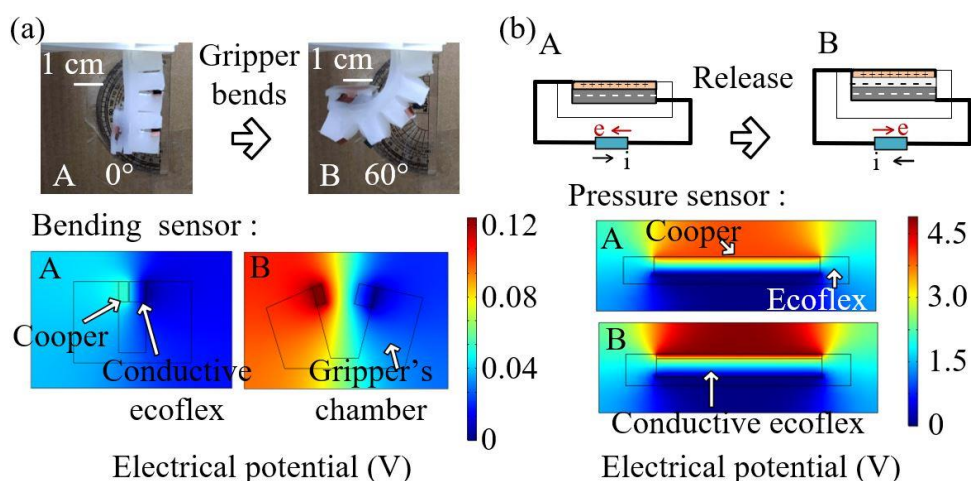


Figure 5.4: Simulation of the potential distribution in the sensors using COMSOL Multiphysics. (a) Simulation result of bend sensor. (b) Simulation result of the pressure sensor.

As mentioned in the preceding section, the separation distance between the triboelectric layers increases when the fingers bend and (state “B”) induces

the electrical potential difference due to the charge transfer mechanism. On the other hand, the pressure sensor reduces the separation distance when an object is gripped. The numerical simulation in Figure 5.4 (b) shows the potential differences when the pressure sensor is released from the pressed state. When the soft gripper grabs an object, the two triboelectric layers become closer and reduce the potential differences. The pressure release increases the separation distance and thus, increases the potential differences. The simulation shows that a gradient in the charge density produces a flow of electrical current according to the separation distance between the two layers.

5.6 Results and Discussions

5.6.1 Characterisation of Pressure Sensor

The characterization of the pressure sensor was conducted using a Shimadzu Servo Pulser E-series (Shimadzu, Kyoto, Japan), which allows the controllable compression motion in the vertical axis. The experiment setup was shown in the inset of Figure 5.5 (a)-(i). The output voltage from the pressure sensor was acquired using a NI Elvis board (NI-ELVIS Series II, USA). Figure 5.5 (a)-(i) summarises the correlation between the input pressure and the output voltage. A polynomial fitting curve and its fitting equation:

$$y = \beta_0 + \beta_1 x + \beta_2 x^2 + \beta_3 x^3 \quad (5.1)$$

is generated in Figure 5.5 (a)-(i) to obtain the numerical relationship between the V_{pp} and input pressure. From equation 5.1, the parameter β_0 is the y-

intercept, β_1 , β_2 and β_3 , are the slope coefficients that determine the error percentage, and x is the corresponding input pressure.

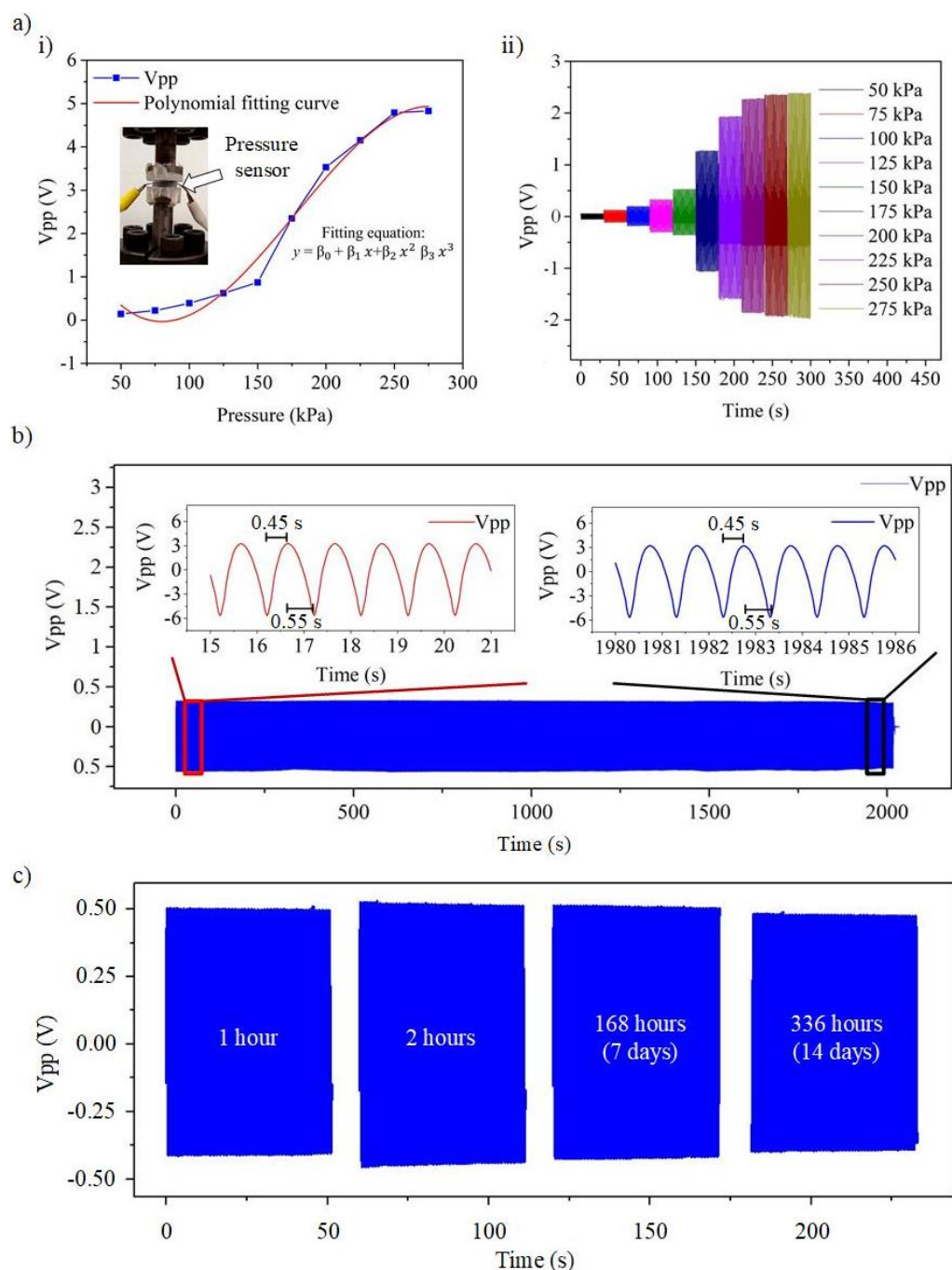


Figure 5.5: (a)-(i) Temporal response of the triboelectric output at different deflections on the pressure sensor ranging from 50 kPa to 275 kPa with an increment of 25 kPa. (a)-(ii) V_{pp} at different input pressure on the pressure sensor. (b) Mechanical durability test under 2200 seconds of continuous mechanical pressing with an input pressure and frequency of 150 kPa and 1 Hz. (c) Stability test of the sensor after 1 hour, 2 hours, 168 hours (7 days) and 336 hours (14 days).

However, it shows a decline on the fitting curve when the input pressure increases more than 250 kPa, representing the sensor's maximum detectable pressure input. Repetitive triboelectric output under an operating frequency of 1 Hz, shown in Figure 5.5 (a)-(ii), proves the consistency and reliability of the pressure sensor in detecting 150 kPa applied pressure. The symmetrical pattern in the positive and negative peaks indicates that the symmetrical structure of the separation distance between the triboelectric layers can return to its original position without any hysteresis. The maximum output voltage reaches $4.82 V_{pp}$, and it is saturated when the input pressure increases beyond 250 kPa. A mechanical robustness test was performed using Shimadzu Servo Pulser to apply a compression force of 150 kPa on the pressure sensor continuously for 2200 seconds with an operating frequency of 1 Hz (shown in Figure 5.5 (b)). The response and recovery time of the sensor were measured to be 0.45 s and 0.55 s, respectively. In addition, it was found that the pressure sensor could generate a stable output voltage of $0.90 V_{pp}$ within 2200 seconds of continuous mechanical pressing without a noticeable change in its response and recovery time. The output voltage, V_{pp} , for the 15th to 22nd and 1980th to 1986th mechanical pressing are shown in the inset of Figure 5.5 (b). To further explore the stability of the sensor, the output voltage of the sensor was measured for 1 hour, 2 hours, 168 hours (7 days) and 336 hours (14 days) under operating frequency and compression force of 1 Hz and 150 kPa, respectively. The response of the sensor is presented in Figure 5.5 (c). It shows no significant change in the output voltage, ensuring good stability and reliability.

5.6.2 Characterisation of the Bend Sensor

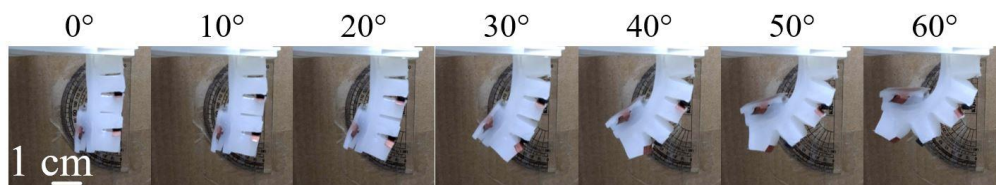


Figure 5.6: The photograph of a single finger bending motion with a bending angle of 0° to 60° (increment of 10°).

The characterisation of the bend sensor was conducted by controlling the input air pressure supplied by a compressor and regulating it using a pressure regulator. The data acquisition was processed utilizing a NI Elvis board (NI-ELVIS Series II, USA). The details of the experiment setup in air pressure regulation will be discussed later. The voltages generated from the bending angle from 0° to 60° with an increment of 10° are quantitatively shown in Figure 5.6.

Figures 5.7 (a) and (b) present the output voltage from the tip and middle bend sensors when they are bent from 0° to 60°. Each angle was repeated three times to ensure the sensors' reliability. Based on the experiments, it can be observed that the generated output voltage is proportional to the bending angle. This can be explained as the separation distance between the two triboelectric layers increases along with the bending angle. Thus, a more significant potential difference was induced. In addition, there are some small positive and negative peaks in each gripping motion. This is due to the vibration from the compressor when injecting or releasing the air pressure. To further explore the stability of the sensor, the output voltage of the tip sensor on the different bending angles was measured for 1 hour, 2 hours, 168 hours (7 days) and 336 hours (14 days).

As presented in Figure 5.7 (c), the average output of the sensor has shown to be consistent within the 14 days, ensuring good stability and reliability.

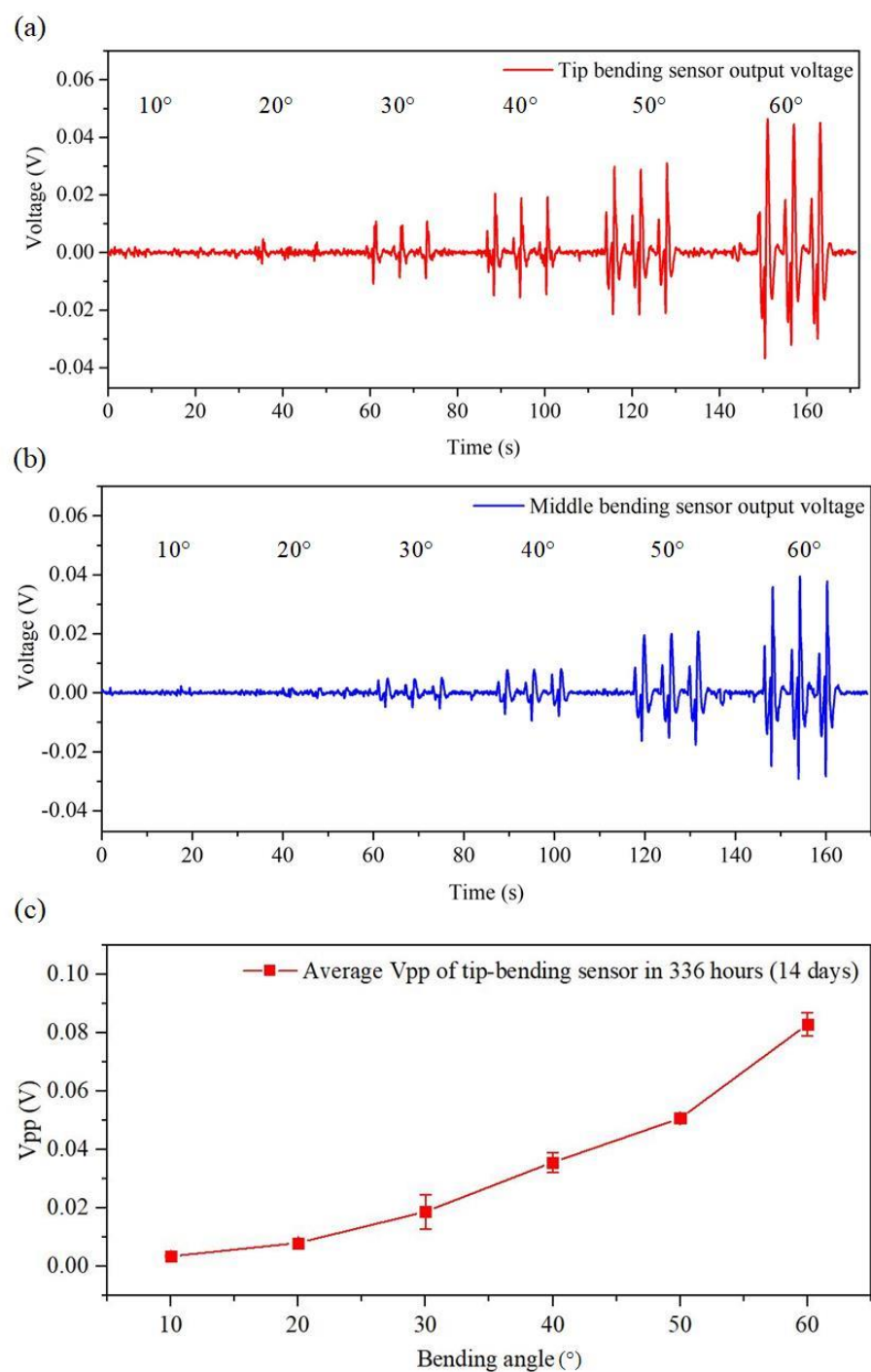


Figure 5.7: (a) The triboelectric output generated by bending the tip sensor from 0° to 60° . (b) The triboelectric output is generated by bending the middle sensor with the bending angle from 0° to 60° . (c) The average voltage output of tip sensor in 336 hours (14 days).

5.7 The Functional Components of the Pick-and-Place System

We mounted the soft gripper on a three-dimensional cartesian manipulator to perform the pick and place operation (Figure 5.8 (a)). The cartesian manipulator was driven by six bipolar stepper motors (NEMA 17 HS4401, China).

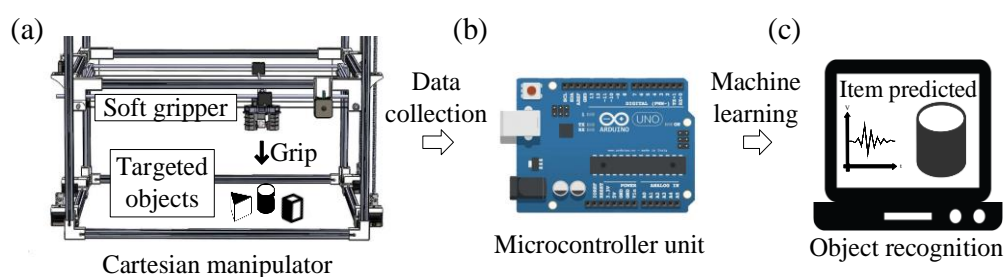


Figure 5.8: The functional components of the pick-and-place system. (a) Cartesian manipulator, (b) Microcontroller unit, (c) Object recognition application.

Four motors control the movement on the Z-axis, and another two motors control the movement on the X and Y-axis. It was programmed via a free, open-sourced software, Printron (Pronterface.com), and controlled by a microcontroller unit (MCU) Arduino Mega 2560 (Figure 5.8 (b)). When an object is gripped, the signal from the sensors is transferred to the MCU and fed into a computer for object recognition (shown in Figure 5.8 (c)). An air compressor (Eurox EAX-5010, Malaysia) was used to activate the opening of the gripper.

5.8 Object Recognition

An experiment was conducted to compare the output generated from a ping pong (diameter = 4 cm) and a softball toy (diameter = 4 cm), as shown in Figure 5.9. The gripping motion was repeated three times to ensure the reliability of the collected result. As shown in Figure 5.9, the output signal of the hard surface shows a higher peak than the soft surface in a grip and release action. The soft gripper experiences higher compression when gripping the hard object, resulting in a more significant change in the separation distance between the two triboelectric layers. Therefore, we can conclude that the soft gripper can recognize soft and hard materials.

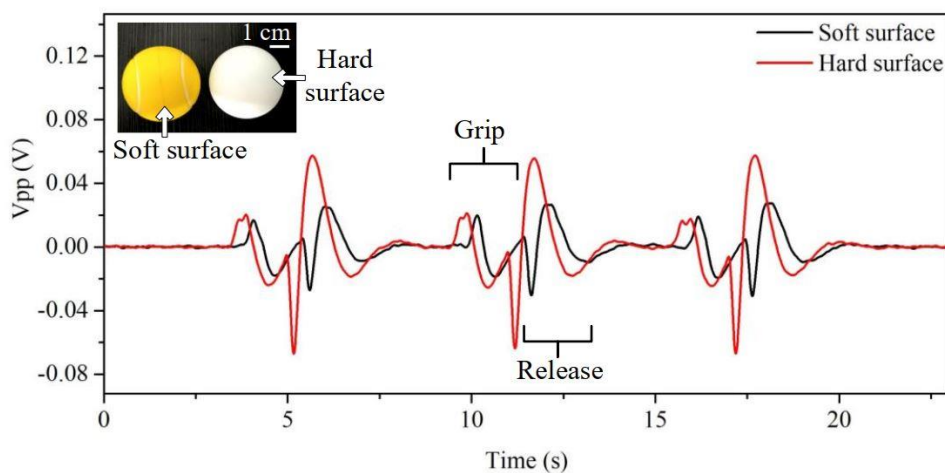


Figure 5.9: Output voltage for two sphere-shaped objects (diameter = 4 cm) with different surface hardness.

The above efforts demonstrate that the pressure and the bend sensors can perceive the bending degree and stiffness of the material. Machine learning (ML) is an advanced technology for gripped object recognition, with massive input signals and extracting features from data sets based on an algorithm.

Amongst the algorithms (such as principal component analysis, random forest, etc.), a support vector machine (SVM) is an efficient supervised learning model used for classification and has been widely applied in analysing triboelectric output signals with high accuracy. In this section, a customized SVM-based recognition platform is developed and applied in our TENG sensors-embedded smart soft gripper. Our TENG sensors are attached directly to the soft gripper, with their positions indicated in Figure 5.10 (a). In addition, six bend sensors, denoted as 1-6, are attached to the Fingers 1-3, coupled with a pressure sensor attached at the tip of each finger. The analog signal generated from the sensors was acquired and processed using the analog to digital converter (ADC) function in an Arduino Mega 2560 microcontroller unit (MCU).

The signal of three objects with different shapes, including a cylindrical, cuboid, and pyramid prism, is collected and analyzed accordingly by repeating the gripping and releasing motions 200 times. The signal collected from the nine sensors for the three objects is visualized in Figure 5.10 (b), and the data length for each sensor is 70. The raw voltage data of the three objects in the time domain are used as the features for SVM training. There are $9 \times 70 = 630$ features for each object during grasping motion. The feature includes the information on the contact pressure, speed, contact duration, etc. The samples are divided into training and testing data with a ratio of 8:2, a total of 160 training data sets and 40 testing data sets.

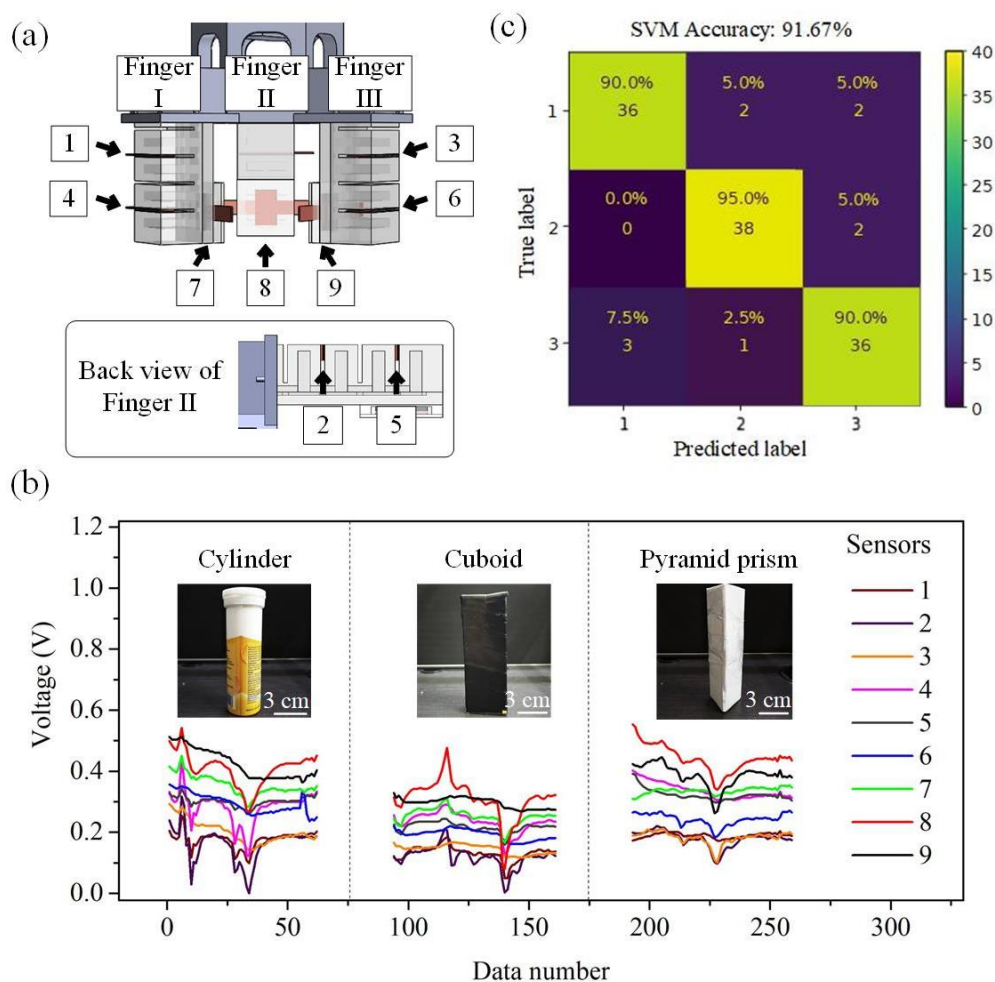


Figure 5.10: (a) Nine sensors (three pressure sensors and six bending angle sensors) are attached to the three fingers. (b) The voltage output of sensors when gripping different objects. (c) The confusion map of the object recognition result.

The confusion matrix in Figure 5.10 (c) shows high accuracy of 91.76%, which is higher than several reported studies with only approximately 84-90% accuracy (Huang et al., 2018; Baghdadi et al., 2018; Babaeian et al., 2016; Winkler-Schwartz et al., 2019; Li et al., 2020). It shows that the developed soft gripper can identify the gripped objects and be further applied to an assembly line for warehouse management in a next-generation smart factory.

5.9 Summary

The TENG-based pressure sensor is successfully implemented in a soft gripper system. It can detect a slight input pressure of 50 kPa and has shown its high robustness and repeatability. No noticeable signal degradation is observed in the sensor's response and recovery time when the pressure sensor is compressed and released for 2200 continuous cycles. Besides the pressure sensor, a bend sensor was successfully developed using the same sponge approach. It can measure the maximum angle change of 60 °. The sensors enable the soft gripper to perform pick-and-place operations and monitor the gripping process without a visual inspection. The data extracted from the gripping process is used for object recognition with high accuracy of 91.67%, which is higher than the several reported studies with only approximately 84-90% accuracy (Huang et al., 2018; Baghdadi et al., 2018; Babaeian et al., 2016; Winkler-Schwartz et al., 2019; Li et al., 2020).

CHAPTER 6

CONCLUSIONS AND FUTURE WORKS

6.1 Conclusions

This dissertation presented the design and development of two soft, self-powered triboelectric-based pressure sensors and proved their working principle through simulation analysis, experiments, and demonstration on several applications. The pressure sensor is designed using a soft elastomer, PDMS, in our first approach. The triboelectrification is achieved based on rubber-liquid interaction. The soft elastomer, as the triboelectric negative layer, induces charge transportation when the liquid flows in the spiral-shaped microchannel at an applied pressure. The pressure sensor can detect an input pressure of 50 kPa and has its robustness tested for 2920 cycles without degradation on the sensor's response and recovery time. With its compact design, it is space-efficient and effective in sensing fingertip pressure. As proof-of-concept demonstration for non-compliance surface integration, the pressure sensor was applied as a touch sensor to control light illumination and gaming interaction for human-machine interaction (HMI) application. Although the TENG-based pressure sensor shows good compliance with the human finger, this design is limited for its saturated output at higher compression strokes, limiting the sensor from sensing larger pressure input sources such as hand tapping motion.

Therefore, to expand the capability of a soft pressure sensor, it is necessary to improve the sensitivity of the pressure sensor.

To improve the output response and sensitivity from pressure sensing, physical modification has been made to the second approach by embedding microporous within the silicone rubber. This modification could increase the contacted surface area and increase the output voltage. A numerical simulation was conducted to quantitatively prove that the potential difference in the porous-based structure is higher than in the non-porous-based structure. To validate the hypothesis, experimental measurements were performed to study the electrical outputs for different porosity: 0%, 25%, 45%, and 65% of total volume. The result shows that the electrical output increases with the porosity value. The SBTENG improves the output voltage, which can power up LEDs by harvesting energy from hand tapping motion.

Upon proving its capability in human pressure sensing, the sponge based TENG pressure sensor is further leveraged for future smart manufacturing. We integrate the TENG based pressure sensor into a soft robotic gripper. A bend sensor is fabricated using the same approach and embedded at the joint of the soft gripper. The bend sensor can detect the soft gripper's bending angle (up to 60 °), whereas the pressure sensor functions to detect the gripped object. By adopting the readout technique of using the peak to peak voltage, the influences of environmental fluctuation, including humidity, temperature, and pressure, can be effectively minimised. With the aid of the AI in processing the complex

multi-parameter inputs, the smart gripper successfully perceives three objects with 91.67% accuracy.

6.2 Future Works

The developed self-powered, stretchable triboelectric pressure sensors have demonstrated their abilities for wearable HMI application and soft robotics' object recognition. Mixing eutectic gallium-indium (EGaIn) in the elastomer has made the triboelectric layer a conductive medium. Nonetheless, both developed soft pressure sensors require flexible but solid copper as connectors, restricting the sensors from achieving the fullest extent of their stretchability. Therefore, for future works, we propose to replace the flexible copper (Young's modulus, $E = 117$ GPa) electrodes with other flexible conductors such as stretchable conductive fabric (Jia et al., 2019), which has a lower young modulus of 36.5 MPa. Thus, it allows the pressure sensors to achieve better stretchability.

The current object recognition system is limited to symmetrical and simple-structured objects due to the lack of sensors in other parts of the soft fingers. Therefore, we propose increasing the sensor numbers and reducing the size to achieve miniaturization for future work. Increasing the sensor can improve the feature extraction of the recognition process. Hence, it can improve recognition accuracy and expand its ability to identify more complex objects. Furthermore, the gripper system can implement digital twin technology to duplicate robotic manipulation in a virtual environment that follows the real-

time operation of the soft-robotic gripper system. With the implementation of the digital twin technology, the soft gripper system can be used for virtual assembly lines and unmanned warehouse applications for energy saving.

REFERENCES

- Abdi, A.M., 2020. Land cover and land use classification performance of machine learning algorithms in a boreal landscape using Sentinel-2 data. *GIScience and Remote Sensing*, 57(1), pp.1–20. Available at: <https://doi.org/10.1080/15481603.2019.1650447>.
- Ahmed, A. et al., 2020. Triboelectric Nanogenerator versus Piezoelectric Generator at Low Frequency (<4 Hz): A Quantitative Comparison. *iScience*, 23(7), p.101286. Available at: <https://doi.org/10.1016/j.isci.2020.101286>.
- Andrejevic, M. and Selwyn, N., 2020. Facial recognition technology in schools: critical questions and concerns. *Learning, Media and Technology*, 45(2), pp.115–128. Available at: <https://doi.org/10.1080/17439884.2020.1686014>.
- Ankanahalli Shankaregowda, S. et al., 2019. Single-electrode triboelectric nanogenerator based on economical graphite coated paper for harvesting waste environmental energy. *Nano Energy*, 66(July), p.104141. Available at: <https://doi.org/10.1016/j.nanoen.2019.104141>.
- Babaeian, M., Bhardwaj, N., Esquivel, B. and Mozumdar, M., 2016. Real time driver drowsiness detection using a logistic-regression-based machine learning algorithm. *2016 IEEE Green Energy and Systems Conference, IGSEC 2016*.
- Baghdadi, A., Megahed, F.M., Esfahani, E.T. and Cavuoto, L.A., 2018. A machine learning approach to detect changes in gait parameters following a fatiguing occupational task. *Ergonomics*, 61(8), pp.1116–1129. Available at: <http://doi.org/10.1080/00140139.2018.1442936>.
- Bai, P. et al., 2013. Integrated multilayered triboelectric nanogenerator for harvesting biomechanical energy from human motions. *ACS Nano*, 7(4), pp.3713–3719.
- Baytekin, H.T., Baytekin, B., Soh, S. and Grzybowski, B.A., 2011. Is water necessary for contact electrification? *Angewandte Chemie - International Edition*, 50(30), pp.6766–6770.
- Belgiu, M. and Drăgu, L., 2016. Random forest in remote sensing: A review of applications and future directions. *ISPRS Journal of Photogrammetry and Remote Sensing*, 114, pp.24–31.
- Chee, P.S. et al., 2012. Modular architecture of a non-contact pinch actuation micropump. *Sensors (Switzerland)*, 12(9), pp.12572–12587.
- Chee, P.S., Minjal, M.N., Leow, P.L. and Ali, M.S.M., 2015. Wireless powered thermo-pneumatic micropump using frequency-controlled heater. *Sensors and Actuators, A: Physical*, 233, pp.1–8. Available at: <http://dx.doi.org/10.1016/j.sna.2015.06.017>.

Chee, P.S., Nafea, M., Leow, P.L. and Ali, M.S.M., 2016. Thermal analysis of wirelessly powered thermo-pneumatic micropump based on planar LC circuit. *Journal of Mechanical Science and Technology*, 30(6), pp.2659–2665.

Chen, J. et al., 2013. Harmonic-resonator-based triboelectric nanogenerator as a sustainable power source and a self-powered active vibration sensor. *Advanced Materials*, 25(42), pp.6094–6099.

Deuschle, J.K., De Souza, E.J., Arzt, E. and Enders, S., 2010. Nanoindentation studies on crosslinking and curing effects of PDMS. *International Journal of Materials Research*, 101(8), pp.1014–1023.

Dharmasena, R.D.I.G., Deane, J.H.B. and Silva, S.R.P., 2018. Nature of Power Generation and Output Optimization Criteria for Triboelectric Nanogenerators. *Advanced Energy Materials*, 8(31).

Dharmasena, R.D.I.G. and Silva, S.R.P., 2019. Towards optimized triboelectric nanogenerators. *Nano Energy*, 62(April), pp.530–549. Available at: <https://doi.org/10.1016/j.nanoen.2019.05.057>.

Diaz, A.F. and Felix-Navarro, R.M., 2004. A semi-quantitative tribo-electric series for polymeric materials: The influence of chemical structure and properties. *Journal of Electrostatics*, 62(4), pp.277–290.

Fan, F.R. et al., 2012. Transparent triboelectric nanogenerators and self-powered pressure sensors based on micropatterned plastic films. *Nano Letters*, 12(6), pp.3109–3114.

Fan, Y.J. et al., 2017. Stretchable Porous Carbon Nanotube-Elastomer Hybrid Nanocomposite for Harvesting Mechanical Energy. *Advanced Materials*, 29(2), pp.1–8.

Gong, J., Xu, B. and Tao, X., 2017. Breath Figure Micromolding Approach for Regulating the Microstructures of Polymeric Films for Triboelectric Nanogenerators. *ACS Applied Materials and Interfaces*, 9(5), pp.4988–4997.

Haleem, A., Vaishya, R., Javaid, M. and Khan, I.H., 2020. Artificial Intelligence (AI) applications in orthopaedics: An innovative technology to embrace. *Journal of Clinical Orthopaedics and Trauma*, 11(xxxx), pp.S80–S81. Available at: <https://doi.org/10.1016/j.jcot.2019.06.012>.

Hildt, E., 2019. Artificial intelligence: Does consciousness matter? *Frontiers in Psychology*, 10(JUL), pp.1–3.

Huang, X. et al., 2018. A novel fault diagnosis system on polymer insulation of power transformers based on 3-stage GA-SA-SVM OFC selection and ABC-SVM classifier. *Polymers*, 10(10).

Jia, L.C. et al., 2019. Stretchable and durable conductive fabric for ultrahigh

performance electromagnetic interference shielding. *Carbon*, 144, pp.101–108. Available at: <https://doi.org/10.1016/j.carbon.2018.12.034>.

Kavzoglu, T., 2017. *Object-Oriented Random Forest for High Resolution Land Cover Mapping Using Quickbird-2 Imagery* 1st ed., Elsevier Inc.

Kavzoglu, T., Bilucan, F. and Teke, A., 2020. COmparison of support vector machines, random forest and decision tree methods for classification of sentinel - 2A image using different band combinations. *ACRS 2020 - 41st Asian Conference on Remote Sensing*, (December).

Ko, Y.H., Nagaraju, G., Lee, S.H. and Yu, J.S., 2014. PDMS-based triboelectric and transparent nanogenerators with ZnO nanorod arrays. *ACS Applied Materials and Interfaces*, 6(9), pp.6631–6637.

Kong, D.S. et al., 2021. A highly efficient and durable kirigami triboelectric nanogenerator for rotational energy harvesting. *Energies*, 14(4).

Lee, J.W., Ye, B.U. and Baik, J.M., 2017. Research Update: Recent progress in the development of effective dielectrics for high-output triboelectric nanogenerator. *APL Materials*, 5(7).

Lee, K.Y. et al., 2014. Hydrophobic sponge structure-based triboelectric nanogenerator. *Advanced Materials*, 26(29), pp.5037–5042.

Lee, M. et al., 2012. A hybrid piezoelectric structure for wearable nanogenerators. *Advanced Materials*, 24(13), pp.1759–1764.

Lei, R. et al., 2020. Sustainable high-voltage source based on triboelectric nanogenerator with a charge accumulation strategy. *Energy and Environmental Science*, 13(7), pp.2178–2190.

Li, G.Z. et al., 2019. High-Performance Transparent and Flexible Triboelectric Nanogenerators Based on PDMS-PTFE Composite Films. *Advanced Electronic Materials*, 5(4), pp.1–8.

Li, Wenjian et al., 2020. Vibrational Triboelectric Nanogenerator-Based. *Ieee/Asme Transactions on Mechatronics*, 25(5), pp.2188–2196.

Lin, B. and Giurgiutiu, V., 2006. Modeling and testing of PZT and PVDF piezoelectric wafer active sensors. *Smart Materials and Structures*, 15(4), pp.1085–1093.

Lin, L. et al., 2013. Segmentally structured disk triboelectric nanogenerator for harvesting rotational mechanical energy. *Nano Letters*, 13(6), pp.2916–2923.

Liu, Z. et al., 2019. Wearable and Implantable Triboelectric Nanogenerators. *Advanced Functional Materials*, 29(20), pp.1–19.

Luo, Y. et al., 2021. Triboelectric bending sensor based smart glove towards intuitive multi-dimensional human-machine interfaces. *Nano Energy*, 89(July), pp.1–9.

Ma, S.W. et al., 2018. Flexible Porous Polydimethylsiloxane/Lead Zirconate Titanate-Based Nanogenerator Enabled by the Dual Effect of Ferroelectricity and Piezoelectricity. *ACS Applied Materials and Interfaces*, 10(39), pp.33105–33111.

Ma, Y., Wang, Z., Yang, H. and Yang, L., 2020. Artificial intelligence applications in the development of autonomous vehicles: A survey. *IEEE/CAA Journal of Automatica Sinica*, 7(2), pp.315–329.

Mohd Ghazali, F.A. et al., 2017. Soft dielectric elastomer actuator micropump. *Sensors and Actuators, A: Physical*, 263, pp.276–284. Available at: <http://dx.doi.org/10.1016/j.sna.2017.06.018>.

Mule, A.R. et al., 2019. Wearable Single-Electrode-Mode Triboelectric Nanogenerator via Conductive Polymer-Coated Textiles for Self-Power Electronics. *ACS Sustainable Chemistry and Engineering*, 7(19), pp.16450–16458.

Nayak, S. et al., 2019. Liquid-metal-elastomer foam for moldable multi-functional triboelectric energy harvesting and force sensing. *Nano Energy*, 64(July), p.103912. Available at: <https://doi.org/10.1016/j.nanoen.2019.103912>.

Nie, J. et al., 2018. Self-Powered Microfluidic Transport System Based on Triboelectric Nanogenerator and Electrowetting Technique. *ACS Nano*, 12(2), pp.1491–1499.

Niu, S. et al., 2014. Theoretical investigation and structural optimization of single-electrode triboelectric nanogenerators. *Advanced Functional Materials*, 24(22), pp.3332–3340.

Okuda, T. and Shoda, S., 2018. AI-based chatbot service for financial industry. *Fujitsu Scientific and Technical Journal*, 54(2), pp.4–8.

Pan, C., Liu, D., Ford, M.J. and Majidi, C., 2020. Ultrastretchable, Wearable Triboelectric Nanogenerator Based on Sedimented Liquid Metal Elastomer Composite. *Advanced Materials Technologies*, 5(11), pp.1–8.

Park, J., Kim, I., Yun, J. and Kim, D., 2021. Liquid-metal embedded sponge-typed triboelectric nanogenerator for omnidirectionally detectable self-powered motion sensor. *Nano Energy*, 89(PB), p.106442. Available at: <https://doi.org/10.1016/j.nanoen.2021.106442>.

Park, J.J., Won, P. and Ko, S.H., 2019. A Review on Hierarchical Origami and Kirigami Structure for Engineering Applications. *International Journal of Precision Engineering and Manufacturing - Green Technology*, 6(1), pp.147–

161. Available at: <https://doi.org/10.1007/s40684-019-00027-2>.

Pisner, D.A. and Schnyer, D.M., 2019. *Support vector machine*, Elsevier Inc.
 Qi, D. et al., 2021. Stretchable Electronics Based on PDMS Substrates. *Advanced Materials*, 33(6), pp.1–25.

Rice, K.M. et al., 2014. Environmental mercury and its toxic effects. *Journal of Preventive Medicine and Public Health*, 47(2), pp.74–83.

Rusli, M.Q.A. et al., 2018. Electromagnetic actuation dual-chamber bidirectional flow micropump. *Sensors and Actuators, A: Physical*, 282, pp.17–27. Available at: <https://doi.org/10.1016/j.sna.2018.08.047>.

Sahu, M. et al., 2021. Porosity modulated piezo-triboelectric hybridized nanogenerator for sensing small energy impacts. *Applied Materials Today*, 22, p.100900. Available at: <https://doi.org/10.1016/j.apmt.2020.100900>.

Sergievskaa, V., 2020. Super Strong Artificial Intelligence and Human Mind. *Procedia Computer Science*, 169(2019), pp.458–460. Available at: <https://doi.org/10.1016/j.procs.2020.02.225>.

Shi, Q., Wang, H., Wang, T. and Lee, C., 2016. Self-powered liquid triboelectric microfluidic sensor for pressure sensing and finger motion monitoring applications. *Nano Energy*, 30(September), pp.450–459. Available at: <http://dx.doi.org/10.1016/j.nanoen.2016.10.046>.

Song, J., Gao, L., Tao, X. and Li, L., 2018. Ultra-flexible and large-area textile-based triboelectric nanogenerators with a sandpaper-induced surface microstructure. *Materials*, 11(11).

Tang, Q. et al., 2019. A strategy to promote efficiency and durability for sliding energy harvesting by designing alternating magnetic stripe arrays in triboelectric nanogenerator. *Nano Energy*, 66(August), p.104087. Available at: <https://doi.org/10.1016/j.nanoen.2019.104087>.

Tang, W. et al., 2015. Liquid-metal electrode for high-performance triboelectric nanogenerator at an instantaneous energy conversion efficiency of 70.6%. *Advanced Functional Materials*, 25(24), pp.3718–3725.

Toyabur Rahman, M. et al., 2020. A highly miniaturized freestanding kinetic-impact-based non-resonant hybridized electromagnetic-triboelectric nanogenerator for human induced vibrations harvesting. *Applied Energy*, 279(July), p.115799. Available at: <https://doi.org/10.1016/j.apenergy.2020.115799>.

Wang, Z.L., Lin, L., Chen, J., Niu, S., Zi, Y. (2016). Triboelectric Nanogenerator: Single-Electrode Mode. In: *Triboelectric Nanogenerators. Green Energy and Technology*. Springer, Cham. https://doi.org/10.1007/978-3-319-40039-6_4

Wang, J., Zi, Y., Li, S. and Chen, X., 2019. High-voltage applications of the triboelectric nanogenerator—Opportunities brought by the unique energy technology. *MRS Energy & Sustainability*, 6(1), pp.1–23.

Wang, S. et al., 2014. Freestanding triboelectric-layer-based nanogenerators for harvesting energy from a moving object or human motion in contact and non-contact modes. *Advanced Materials*, 26(18), pp.2818–2824.

Wang, X. et al., 2015. Piezoelectric-Enhanced Oriented Cobalt Coordinated Peptide Monolayer with Rectification Behavior. *Small*, 11(37), pp.4864–4869.

Wang, Z.L., 2012. Self-powered nanosensors and nanosystems. *Advanced Materials*, 24(2), pp.280–285.

Wang, Z.L., 2014. Triboelectric nanogenerators as new energy technology and self-powered sensors - Principles, problems and perspectives. *Faraday Discussions*, 176, pp.447–458.

Wen, F. et al., 2020. Machine Learning Glove Using Self-Powered Conductive Superhydrophobic Triboelectric Textile for Gesture Recognition in VR/AR Applications. *Advanced Science*, 7(14), pp.1–15.

Winkler-Schwartz, A. et al., 2019. Machine Learning Identification of Surgical and Operative Factors Associated with Surgical Expertise in Virtual Reality Simulation. *JAMA Network Open*, 2(8).

Wu, C. et al., 2018. Keystroke dynamics enabled authentication and identification using triboelectric nanogenerator array. *Materials Today*, 21(3), pp.216–222. Available at: <https://doi.org/10.1016/j.mattod.2018.01.006>.

Wu, C. et al., 2019. Triboelectric Nanogenerator: A Foundation of the Energy for the New Era. *Advanced Energy Materials*, 9(1), pp.1–25.

Xiao, T.X. et al., 2018. Silicone-Based Triboelectric Nanogenerator for Water Wave Energy Harvesting. *ACS Applied Materials and Interfaces*, 10(4), pp.3616–3623.

Xu, C. et al., 2018. On the Electron-Transfer Mechanism in the Contact-Electrification Effect. *Advanced Materials*, 30(15), pp.1–9.

Yang, Q., 2018. Internet of things application in smart grid: A brief overview of challenges, opportunities, and future trends. *Smart Power Distribution Systems: Control, Communication, and Optimization*, (April), pp.267–283.

Yang, X. and Daoud, W.A., 2018. Design parameters impact on output characteristics of flexible hybrid energy harvesting generator: Experimental and theoretical simulation based on a parallel hybrid model. *Nano Energy*, 50(March), pp.794–806. Available at: <https://doi.org/10.1016/j.nanoen.2018.05.073>.

Yang, Y. et al., 2018. Liquid-Metal-Based Super-Stretchable and Structure-Designable Triboelectric Nanogenerator for Wearable Electronics. *ACS Nano*, 12(2), pp.2027–2034.

Zhang, L. et al., 2020. Free-standing triboelectric layer-based full fabric wearable nanogenerator for efficient mechanical energy harvesting. *ACS Applied Electronic Materials*, 2(10), pp.3366–3372.

Zhang, M. et al., 2016. Robust design of unearthed single-electrode TENG from three-dimensionally hybridized copper/polydimethylsiloxane film. *Nano Energy*, 30(October), pp.155–161. Available at: <http://dx.doi.org/10.1016/j.nanoen.2016.10.002>.

Zhang, W. et al., 2020. Multilanguage-handwriting self-powered recognition based on triboelectric nanogenerator enabled machine learning. *Nano Energy*, 77(July), p.105174. Available at: <https://doi.org/10.1016/j.nanoen.2020.105174>.

Zhao, L. et al., 2016. A size-unlimited surface microstructure modification method for achieving high performance triboelectric nanogenerator. *Nano Energy*, 28, pp.172–178.

Zheng, Y. et al., 2014. An electrospun nanowire-based triboelectric nanogenerator and its application in a fully self-powered UV detector. *Nanoscale*, 6(14), pp.7842–7846.

Zhu, G. et al., 2012. Triboelectric-generator-driven pulse electrodeposition for micropatterning. *Nano Letters*, 12(9), pp.4960–4965.

Zi, Y., Wu, C., Ding, W. and Wang, Z.L., 2017. Maximized Effective Energy Output of Contact-Separation-Triggered Triboelectric Nanogenerators as Limited by Air Breakdown. *Advanced Functional Materials*, 27(24), pp.1–8.

Zou, H. et al., 2019. Quantifying the triboelectric series. *Nature Communications*, 10(1), pp.1–9.



PUBLICATIONS

- a) Goh, Q.L., Chee, P.S., Lim, E.H. and Liew, G.G., 2021. Self-powered pressure sensor based on microfluidic triboelectric principle for human-machine interface applications. *Smart Materials and Structures*, 30(7), p.75012. Available at: <https://doi.org/10.1088/1361-665X/ac01a5>.
- b) Goh, Q.L., Chee, P.S. and Lim, E.H., 2021. A Parametric Study of a Sponge-based Triboelectric Energy Harvester. *Proceedings - 2020 IEEE EMBS Conference on Biomedical Engineering and Sciences, IECBES 2020*, (i), pp.158–161.
- c) Goh, Q.-L., Chee, P.-S., Lim, E.-H. and Ng, D.W.-K., 2022. An AI-Assisted and Self-Powered Smart Robotic Gripper Based on Eco-EGaIn Nanocomposite for Pick-and-Place Operation. *Nanomaterials*, 12(8). Available at: <https://www.mdpi.com/2079-4991/12/8/1317>.

APPENDICES

APPENDIX A: Ethical Approval for Research Project

Page 1 of Ethical Approval Letter

 UNIVERSITI TUNKU ABDUL RAHMAN <small>Wholly Owned by UTAR Education Foundation (Company No. 578227-00)</small>	
Re: U/SERC/219/2021	
28 September 2021	
Dr Chee Pei Song Department of Mechatronics and BioMedical Engineering Lee Kong Chian Faculty of Engineering and Science Universiti Tunku Abdul Rahman Jalan Sungai Long Bandar Sungai Long 43000 Kajang, Selangor	
Dear Dr Chee,	
Ethical Approval For Research Project/Protocol	
We refer to your application for ethical approval for your research project (Master student's project) and are pleased to inform you that your application has been approved under <u>Expedited Review</u> .	
The details of your research project are as follows:	
Research Title	Design and Development of Stretchable Energy Harvesters
Investigator(s)	Dr Chee Pei Song Goh Qi Lum (UTAR Postgraduate Student)
Research Area	Science
Research Location	UTAR
No of Participants	1 participant
Research Costs	MOHE Fundamental Research Grant Scheme (MOHE FRGS)
Approval Validity	28 September 2021 - 27 September 2022
The conduct of this research is subject to the following:	
<ol style="list-style-type: none"> (1) The participants' informed consent be obtained prior to the commencement of the research; (2) Confidentiality of participants' personal data must be maintained; and (3) Compliance with procedures set out in related policies of UTAR such as the UTAR Research Ethics and Code of Conduct, Code of Practice for Research Involving Humans and other related policies/guidelines. (4) Written consent be obtained from the institution(s)/company(ies) in which the physical or/and online survey will be carried out, prior to the commencement of the research. 	
<small> Kampus Kampar : Jalan Universiti, Bandar Barat, 31900 Kampar, Perak Darul Ridzuan, Malaysia Tel: (607) 462 3333 Fax: (607) 466 1313 Sungai Long Campus : Jalan Sungai Long, Bandar Sungai Long, Cheras, 43000 Kajang, Selangor Darul Ehsan, Malaysia Tel: (603) 9086 0155 Fax: (603) 9019 5565 Website: www.utar.edu.my </small>	
	

Page 2 of Ethical Approval Letter

Should you collect personal data of participants in your study, please have the participants sign the attached Personal Data Protection Statement for your records.

The University wishes you all the best in your research.

Thank you.

Yours sincerely,



Professor Ts Dr Faiz bin Abd Rahman
Chairman
UTAR Scientific and Ethical Review Committee

c.c Dean, Lee Kong Chian Faculty of Engineering and Science
Director, Institute of Postgraduate Studies and Research

Kampar Campus : Jalan Universiti, Bandar Barat, 31900 Kampar, Perak Darul Ridzuan, Malaysia
Tel: (607) 468 8888 Fax: (607) 466 1313
Sungai Long Campus : Jalan Sungai Long, Bandar Sungai Long, Cheras, 43000 Kajang, Selangor Darul Ehsan, Malaysia
Tel: (603) 9086 0288 Fax: (603) 9019 8868
Website: www.utar.edu.my



APPENDIX B: 1st page of Turnitin originality report

Document Viewer

Turnitin Originality Report

Processed on: 24-Apr-2022 18:21 +08
 ID: 1818549911
 Word Count: 15518
 Submitted: 1

Similarity Index 8%	Similarity by Source Internet Sources: 3% Publications: 7% Student Papers: 1%
--	---

GOH QI LUN_20UED00165_Thesis Revised By
 Goh Qi Lun

[include quoted](#) [include bibliography](#) [excluding matches < 8 words](#) mode: quickview (classic) report

Change mode [print](#) [download](#)

1% match (publications)
[Tao Jin, Zhongda Sun, Long Li, Qian Zhang et al. "Triboelectric nanogenerator sensors for soft robotics aiming at digital twin applications", Nature Communications, 2020](#)

1% match (publications)
["Micro Electro Mechanical Systems", Springer Science and Business Media LLC, 2018](#)

<1% match (Internet from 02-Sep-2014)
<http://onlinelibrary.wiley.com>

<1% match (publications)
[Wenlian Li, Yaoyao Liu, Shuwei Wang, Wei Li, Guoxu Liu, Junging Zhao, Xiaohan Zhang, Chi Zhang, "Vibrational Triboelectric Nanogenerator-based Multi-node Self-powered Sensor Network for Machine Fault Detection", IEEE/ASME Transactions on Mechatronics, 2020](#)

<1% match (Internet from 11-Sep-2020)
<https://www.hindawi.com/journals/jnm/2016/5651613/>

<1% match (Internet from 19-Jul-2021)
<https://aclanthology.org/2020/pacli-1.pdf>

<1% match (publications)
[Sung Soo Kwak, Hong-Joon Yoon, Sang-Woo Kim, "Textile-Based Triboelectric Nanogenerators for Self-Powered Wearable Electronics", Advanced Functional Materials, 2019](#)

<1% match (Internet from 18-Oct-2021)
https://uwspace.uwaterloo.ca/bitstream/handle/10012/14158/Mahmud_Alam.pdf?isAllowed=y&sequence=3

<1% match (publications)
[Peng Yang, Yuxiang Shi, Shuyao Li, Xinglin Tao, Zhaogui Liu, Xingling Wang, Zhong Lin Wang, Xiangyu Chen, "Monitoring the Degree of Comfort of Shoes In-Motion Using Triboelectric Pressure Sensors with an Ultrawide Detection Range", ACS Nano, 2022](#)

<1% match (publications)
[Yang Luo, Zihan Wang, Jiyu Wang, Xiao Xiao, Qian Li, Wenbo Ding, H.Y. Fu, "Triboelectric bending sensor based smart glove towards intuitive multi-dimensional human-machine interfaces", Nano Energy, 2021](#)

<1% match (publications)
[Chuanyu Bu, Fujiang Li, Kai Yin, Jinbo Pang, Licheng Wang, Kai Wang, "Research Progress and Prospect of Triboelectric Nanogenerators as Self-Powered Human Body Sensors", ACS Applied Electronic Materials, 2020](#)

<1% match (Internet from 20-Nov-2015)
<http://www.researchgate.net>

<1% match (Internet from 04-Jan-2021)
https://www.researchgate.net/publication/294577401_Random_forest_in_remote_sensing_A_review_of_applications_and_fu

<1% match (student papers from 13-Dec-2019)
[Submitted to Xiamen University on 2019-12-13](#)